



ATLAS Note

GROUP-2017-XX

1st September 2020



1

2 WZ + Heavy Flavor Production in pp collisions 3 at $\sqrt{s} = 13$ TeV

4

The ATLAS Collaboration

5

A measurement of WZ produced with an associated heavy flavor jet is performed using 140
6 fb^{-1} of proton-proton collision data at $\sqrt{s} = 13$ TeV from the ATLAS experiment at the
7 LHC. The measurement is performed in the fully leptonic decay mode, $\text{WZ} \rightarrow \ell\bar{\nu}\ell\bar{\nu}$. The
8 cross-section of $\text{WZ} + b\text{-jets}$ is measured to be $X \pm X \pm X$, while the cross-section of $\text{WZ} +$
9 charm is measured as X , with a correlation of X between the two processes.

10

© 2020 CERN for the benefit of the ATLAS Collaboration.

Reproduction of this article or parts of it is allowed as specified in the CC-BY-4.0 license.

¹¹ **Contents**

¹² **1 Changes and outstanding items**

¹³ **1.1 Changelog**

¹⁴ This is version 3

¹⁵ **1.1.1 Changes relative to v2**

- ¹⁶ • Included a section on tZ interference effects, ??.
- ¹⁷ • Updated to reflect changes for 2018, including the move to PFlow jets, DL1r, updated trigger, and updated AnalysisBase version (now 21.2.127)

¹⁹ **1.1.2 Changes relative to v1**

- ²⁰ • Added GRL list
- ²¹ • Fixed latex issue in line 92, typo in line 172
- ²² • Added tables [6](#) and [4](#), summarizing the event and object selection
- ²³ • Added table [2](#), which includes the DSID of samples used
- ²⁴ • Included reference to WZ inclusive paper in introduction

²⁵ **1.2 Outstanding Items**

- ²⁶ • Include new Madgraph WZjj VBS samples - currently using Sherpa, which is missing b-jet diagrams
- ²⁸ • Move to updated 2018 data and MC recommendations
- ²⁹ • Understand data/MC discrepancies, likely from fake contribution. Possibly move to data driven fakes
- ³¹ • Investigate VVV samples, ensure no overlap with WZjj samples
- ³² • Include selection to reject events with a fourth soft lepton to reduce ZZ->llll contribution
- ³³ • Add details on top mass reconstruction, specifically to justify choices made

34 2 Introduction

35 The production of WZ in association with a heavy flavor jet represents an important background
 36 for many major analyses. This includes any process with leptons and b-jets in the final state,
 37 such as $t\bar{t}H$, $t\bar{t}W$, and $t\bar{t}Z$. While precise measurements have been made of WZ production
 38 [1], $WZ +$ heavy flavor remains poorly understood. This is largely because the QCD processes
 39 involved in the production of the b-jet make it difficult to simulate accurately. This introduces a
 40 large uncertainty for analyses that include this process as a background.

41 Motivated by its relevance to the $t\bar{t}H$ multilepton analysis, we perform a study of the fully
 42 leptonic decay mode of this channel; that is, events where both the W and Z decay leptonically.
 43 Because WZ has no associated jets at leading order, while the major backgrounds for this channel
 44 tend to have high jet multiplicity, events with more than two jets are rejected. This gives a final
 45 state signature of three leptons and one or two jets.

46 Events that meet this selection criteria are sorted into pseudo-continuous b-tagging regions based
 47 on the DL1r b-tag score of their associated jets. This is done to separate $WZ +$ b-jet events from
 48 $WZ +$ charm and $WZ +$ light jets. These regions are fit to data in order make a more accurate
 49 estimate of the contribution of $WZ +$ heavy-flavor, where heavy-flavor jets include b-jets and
 50 charm jets. The full Run-2 dataset collected by the ATLAS detector, representing 139 fb^{-1} of
 51 data from pp collisions at $\sqrt{s} = 13 \text{ TeV}$, is used for this study.

52 Section 3 details the data and Monte Carlo (MC) samples used in the analysis. The reconstruction
 53 of various physics objects is described in section 4. Section 5 describes the event selection applied
 54 to these samples. The multivariate analysis techniques used to separate the tZ background from
 55 $WZ +$ heavy flavor are described in section ???. The regions defined for the fit are then described
 56 in section ???. Section ?? describes the various sources of systematic uncertainties considered
 57 in the fit. Finally, the results of the analysis are summarized in section ??, followed by a brief
 58 conclusion in section ??.

59 **The current state of the analysis shows blinded results for the full 2018 dataset, awaiting**
 60 **unblinding approval.**

61 3 Data and Monte Carlo Samples

62 Both data and Monte Carlo samples used in this analysis were prepared in the xAOD format,
 63 which was used to produce a Dx AOD sample in the HIGG8D1 derivation framework. The HIGG8D1
 64 framework is designed for the $t\bar{t}H$ multi-lepton analysis, which targets events with multiple
 65 leptons as well as tau hadrons. This framework skims the dataset to remove unneeded variables
 66 as well as entire events. Events are removed from the derivations that do not meet the following
 67 selection:

- 68 • at least two light leptons within a range $|\eta| < 2.6$, with leading lepton $p_T > 15 \text{ GeV}$ and
 69 subleading lepton $p_T > 5 \text{ GeV}$

- 70 • at least one light lepton with $p_T > 15$ GeV within a range $|\eta| < 2.6$, and at least two hadronic
 71 taus with $p_T > 15$ GeV.

72 Samples were then generated from these HIGG8D1 derivations using a modified version of
 73 AnalysisBase version 21.2.127.

74 **3.1 Data Samples**

75 The study uses a sample of proton-proton collision data collected by the ATLAS detector from
 76 2015 through 2018 at an energy of $\sqrt{s} = 13$ TeV, which represents an integrated luminosity of
 77 139 fb^{-1} . This data set was collected with a bunch crossing rate of 25 ns. All data used in this
 78 analysis was verified by data quality checks, having been included in the following Good Run
 79 Lists:

- 80 • data15_13TeV.periodAllYear_DetStatus-v79-repro20-02_DQDefects-00-02-02
 81 _PHYS_StandardGRL_All_Good_25ns.xml
- 82 • data16_13TeV.periodAllYear_DetStatus-v88-pro20-21_DQDefects-00-02-04
 83 _PHYS_StandardGRL_All_Good_25ns.xml
- 84 • data17_13TeV.periodAllYear_DetStatus-v97-pro21-13_Uncknown_PHYS_StandardGRL
 85 _All_Good_25ns_Triggerno17e33prim.xml
- 86 • data18_13TeV.periodAllYear_DetStatus-v102-pro22-04_Uncknown_PHYS_StandardGRL
 87 _All_Good_25ns_Triggerno17e33prim.xml

88 **3.2 Monte Carlo Samples**

89 Several different generators were used to produce Monte Carlo simulations of the signal and
 90 background processes. For all samples, the response of the ATLAS detector is simulated using
 91 Geant4. The WZ signal samples are simulated using Sherpa 2.2.2 [2]. Specific information
 92 about the Monte Carlo samples being used can be found in table 1. A list of the specific samples
 93 used by data set ID is shown in table ??.

Table 1: The configurations used for event generation of signal and background processes, including the event generator, matrix element (ME) order, parton shower algorithm, and parton distribution function (PDF).

Process	Event generator	ME order	Parton Shower	PDF
WZ, VV	SHERPA 2.2.2	MEPS NLO	SHERPA	CT10
tZ	MG5_AMC	LO	PYTHIA 6	CTEQ6L1
t̄W	MG5_AMC (SHERPA 2.1.1)	NLO (LO multileg)	PYTHIA 8 (SHERPA)	NNPDF 3.0 NLO (NNPDF 3.0 NLO)
t̄(Z/γ* → ll)	MG5_AMC	NLO	PYTHIA 8	NNPDF 3.0 NLO
t̄H	MG5_AMC (MG5_AMC)	NLO (NLO)	PYTHIA 8 (HERWIG++)	NNPDF 3.0 NLO [Ball:2014uwa] (CT10 [ct10])
tHqb	MG5_AMC	LO	PYTHIA 8	CT10
tHW	MG5_AMC (SHERPA 2.1.1)	NLO (LO multileg)	HERWIG++ (SHERPA)	CT10 (NNPDF 3.0 NLO)
tWZ	MG5_AMC	NLO	PYTHIA 8	NNPDF 2.3 LO
t̄t, t̄t̄t̄	MG5_AMC	LO	PYTHIA 8	NNPDF 2.3 LO
t̄W+W-	MG5_AMC	LO	PYTHIA 8	NNPDF 2.3 LO
t̄t	Powheg-BOX v2 [powheggtt]	NLO	PYTHIA 8	NNPDF 3.0 NLO
t̄t̄γ	MG5_AMC	LO	PYTHIA 8	NNPDF 2.3 LO
s-, t-channel, Wt single top	Powheg-BOX v1 [powhegstp]	NLO	PYTHIA 6	CT10
qqVV, VVV Z → l+l-	SHERPA 2.2.1	MEPS NLO	SHERPA	NNPDF 3.0 NLO

4 Object Reconstruction

All regions defined in this analysis share a common lepton, jet, and overall event preselection. This preselection is detailed here; the selection used to define the various fit regions is described in section ??.

4.1 Trigger

Events are required to be selected by dilepton triggers, as summarized in table 3.

4.2 Light leptons

Electron candidates are reconstructed from energy clusters in the electromagnetic calorimeter that are associated with charged particle tracks reconstructed in the inner detector [3]. Electron candidates are required to have $p_T > 10$ GeV and $|\eta_{\text{cluster}}| < 2.47$. Candidates in the transition region between different electromagnetic calorimeter components, $1.37 < |\eta_{\text{cluster}}| < 1.52$, are rejected. A multivariate likelihood discriminant combining shower shape and track information is used to distinguish real electrons from hadronic showers (fake electrons). To further reduce

Sample	DSID
WZ	364253, 364739-42
VV	364250, 364254, 364255, 363355-60, 364890
t̄W	410155
t̄Z	410156, 410157, 410218-20
low mass t̄Z	410276-8
Rare Top	410397, 410398, 410399
single Top	410658-9, 410644-5
three Top	304014
four Top	410080
t̄WW	410081
Z + jets	364100-41
low mass Z + jets	364198-215
W + jets	364156-97
Vγ	364500-35
tZ	410560
tW	410013-4
WtZ	410408
VVV	364242-9
VH	342284-5
WtH	341998
t̄tγ	410389
t̄t	410470
t̄tH	345873-5, 346343-5

Table 2: List of Monte Carlo samples by data set ID used in the analysis.

the non-prompt electron contribution, the track is required to be consistent with originating from the primary vertex; requirements are imposed on the transverse impact parameter significance ($|d_0|/\sigma_{d_0}$) and the longitudinal impact parameter ($|\Delta z_0 \sin \theta_\ell|$), as shown in table 4.

Muon candidates are reconstructed by combining inner detector tracks with track segments or full tracks in the muon spectrometer [4]. Muon candidates are required to have $p_T > 10$ GeV and $|\eta| < 2.5$.

All leptons are required to be isolated, and pass a non-prompt BDT selection described in detail in [5].

4.3 Jets

Jets are reconstructed from calibrated topological clusters built from energy deposits in the calorimeters [6], using the anti- k_t algorithm with a radius parameter $R = 0.4$. Jets with energy contributions likely arising from noise or detector effects are removed from consideration [7],

Dilepton triggers (2015)	
$\mu\mu$ (asymm.)	HLT_mu18_mu8noL1
ee (symm.)	HLT_2e12_lhloose_L12EM10VH
$e\mu, \mu e$ (\sim symm.)	HLT_e17_lhloose_mu14
Dilepton triggers (2016)	
$\mu\mu$ (asymm.)	HLT_mu22_mu8noL1
ee (symm.)	HLT_2e17_lhvloose_nod0
$e\mu, \mu e$ (\sim symm.)	HLT_e17_lhloose_nod0_mu14
Dilepton triggers (2017)	
$\mu\mu$ (asymm.)	HLT_mu22_mu8noL1
ee (symm.)	HLT_2e24_lhvloose_nod0
$e\mu, \mu e$ (\sim symm.)	HLT_e17_lhloose_nod0_mu14
Dilepton triggers (2018)	
$\mu\mu$ (asymm.)	HLT_mu22_mu8noL1
ee (symm.)	HLT_2e24_lhvloose_nod0
$e\mu, \mu e$ (\sim symm.)	HLT_e17_lhloose_nod0_mu14

Table 3: List of lowest p_T -threshold, un-prescaled dilepton triggers used for 2015–2018 data taking.

and only jets satisfying $p_T > 25$ GeV and $|\eta| < 2.5$ are used in this analysis. For jets with $p_T < 60$ GeV and $|\eta| < 2.4$, a jet-track association algorithm is used to confirm that the jet originates from the selected primary vertex, in order to reject jets arising from pileup collisions [8].

4.4 B-tagged Jets

In order to make a measurement of $WZ +$ heavy flavor it is necessary to distinguish these events from $WZ +$ light jets. For this purpose, the DL1r b-tagging algorithm is used to distinguish heavy flavor jets from lighter ones. The DL1r algorithm uses jet kinematics, particularly jet vertex information, as input for a neural network which assigns each jet a score designed to reflect how likely that jet is to have originated from a b-quark.

	e			μ		
	L	L^*	T	L	L^*	T
FixedCutLoose	No	Yes		No	Yes	
Non-prompt lepton BDT	No	Yes		No	Yes	
Identification	Loose	Tight		Loose	Medium	
Charge mis-assignment veto	No	Yes		N/A		
ambiguity bit == 0	No	Yes		N/A		
Transverse impact parameter significance $ d_0 /\sigma_{d_0}$	< 5			< 3		
Longitudinal impact parameter $ z_0 \sin \theta $	$< 0.5 \text{ mm}$					

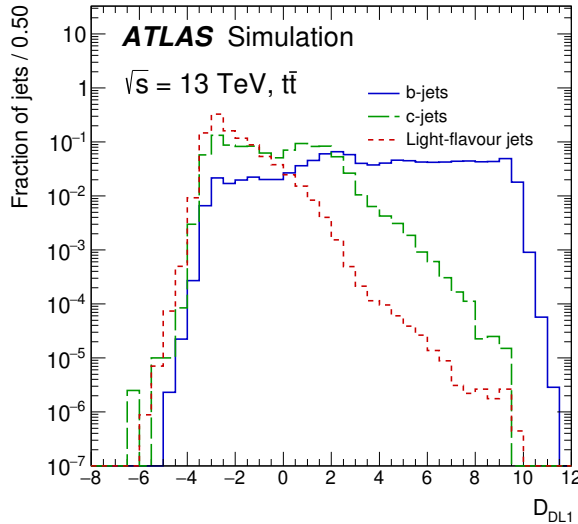
Table 4: Loose (L), loose and minimally-isolated (L^*), and tight (T) light lepton definitions.

Figure 1: Output distribution of the DL1r algorithm for b-jets, charm jets, and light jets

From the output of the BDT, working points (WPs) are developed based on the efficiency of truth b-jets at particular values of the DL1r algorithm. The working points used in this analysis are summarized in table 5.

WP	none	loose	medium	tight	tightest
b eff.	-	85%	77%	70%	60%

Table 5: B-tagging Working Points by tightness and b-jet efficiency

132 A tighter WP will accept fewer b-jets, but reject a higher fraction of charm and light jets.
 133 Generally, analyses that include b-jets will use a fixed working point, for example, requiring that
 134 a jet pass the 70% threshold. By instead treating these working point as bins, e.g. events with
 135 jets that fall between the 85% and 77% WPs fall into one bin, while events with jets passing the
 136 60% WP fall into another, and looking at the full psuedo-continuous DL1r spectrum of the jets,
 137 additional information can be gained. The psuedo-continuous b-tag spectrum is used in this case
 138 to separate out $WZ + b$, $WZ + \text{charm}$, and $WZ + \text{light}$.

139 **4.5 Missing transverse energy**

140 Missing transverse momentum (E_T^{miss}) is used as part of the event selection. The missing
 141 transverse momentum vector is defined as the inverse of the sum of the transverse momenta of
 142 all reconstructed physics objects as well as remaining unclustered energy, the latter of which is
 143 estimated from low- p_T tracks associated with the primary vertex but not assigned to a hard object
 144 [9].

145 **5 Event Selection**

146 Selected events are required to include exactly three reconstructed light leptons passing the
 147 requirement described in 4.2, which have a total charge of ± 1 . As the opposite sign lepton is
 148 found to be prompt the vast majority of the time [5], it is required to be loose and isolated, as
 149 defined though the standard `isolationFixedCutLoose` working point supported by combined
 150 performance groups. The same sign leptons are required to be very tight, as per the recommended
 151 `isolationFixedCutTight`.

152 The leptons are ordered in the analysis code as 0, 1, and 2. Lepton 0 is the lepton whose charge
 153 is opposite the other two. Lepton 1 is the lepton closest to the opposite charge lepton, i.e. the
 154 smallest ΔR , leaving lepton 2 as the lepton further from the opposite charge lepton. Lepton 0
 155 is required to have $p_T > 10 \text{ GeV}$, while the same sign leptons, 1 and 2, are required to have
 156 $p_T > 20 \text{ GeV}$ to reduce the contribution of non-prompt leptons.

157 The invariant mass of at least one pair of opposite sign, same flavor leptons is required to fall
 158 within 10 GeV of the mass of the Z boson, 91.2 GeV. Events where one of the opposite sign pairs
 159 have an invariant mass less than 12 GeV are rejected in order to suppress low mass resonances.

160 An additional requirement is placed on the missing transverse energy, $E_T^{\text{miss}} > 20 \text{ GeV}$, and the
 161 transverse mass of the W candidate, $m(E_T^{\text{miss}} + l_{\text{other}}) > 30 \text{ GeV}$, where E_T^{miss} is the missing
 162 transverse energy, and l_{other} is the lepton not included in the Z-candidate.

163 Events are required to have one or two reconstructed jets passing the selection described in
 164 section 4.3. Events with more than two jets are rejected in order to reduce the contribution of
 165 backgrounds such as $t\bar{t}Z$ and $t\bar{t}W$, which tend to have higher jet multiplicity. This selection of
 166 summarized in table 6.

Event Selection
Exactly three leptons with charge ± 1
Two same-charge leptons with $p_T > 20 \text{ GeV}$
One opposite charge lepton with $p_T > 10 \text{ GeV}$
$m(l^+l^-)$ within 10 GeV of 91.2 GeV
Transverse mass of W-candidate, $m_T(E_T^{\text{miss}} + \text{lep}_{\text{other}}) > 30 \text{ GeV}$
Missing transverse energy, $E_T^{\text{miss}} > 20 \text{ GeV}$
One or two jets with $p_T > 25 \text{ GeV}$

Table 6: Summary of the selection applied to events for inclusion in the fit

167 **5.1 Signal Region Validation**

168 The event yields for both data and Monte Carlo are summarized in table 8, which shows good
 169 agreement between data and Monte Carlo, and demonstrates that this signal region consists
 170 primarily of WZ events.

Process	Events
WZ + b	143.5 ± 3.3
WZ + charm	892.3 ± 9.5
WZ + light	5952.6 ± 26.9
Other VV + b	24.3 ± 1.0
Other VV + charm	33.7 ± 1.3
Other VV + light	487.4 ± 5.8
t̄W	15.2 ± 0.52
t̄tZ	56.1 ± 0.9
rare Top	3.8 ± 0.2
Z + jets	301.7 ± 27.1
V + γ	18.2 ± 8.0
tZ	106.9 ± 2.3
tW	8.7 ± 2.4
WtZ	24.6 ± 1.5
VVV	11.9 ± 0.22
VH	21.7 ± 4.5
t̄t	320.9 ± 12.3
t̄tH	5.2 ± 0.2
Total	8435.66 ± 42.93
Data	8640

Table 7: Events yields at 138.9 fb^{-1} Table 8: Data and MC yields after the event selection requiring three leptons, one or two jets, $E_T^{\text{miss}} > 20 \text{ GeV}$, and $m(E_T^{\text{miss}} + l_{\text{other}}) > 30 \text{ GeV}$ has been applied.

¹⁷¹ Here Other VV represents diboson processes other than WZ, and consists predominantly of
¹⁷² $ZZ \rightarrow ll\bar{l}\bar{l}$ events where one of the leptons is not reconstructed.

¹⁷³ Simulations are further validated by comparing the kinematic distributions of the Monte Carlo
¹⁷⁴ with data, which are shown in figure 4.

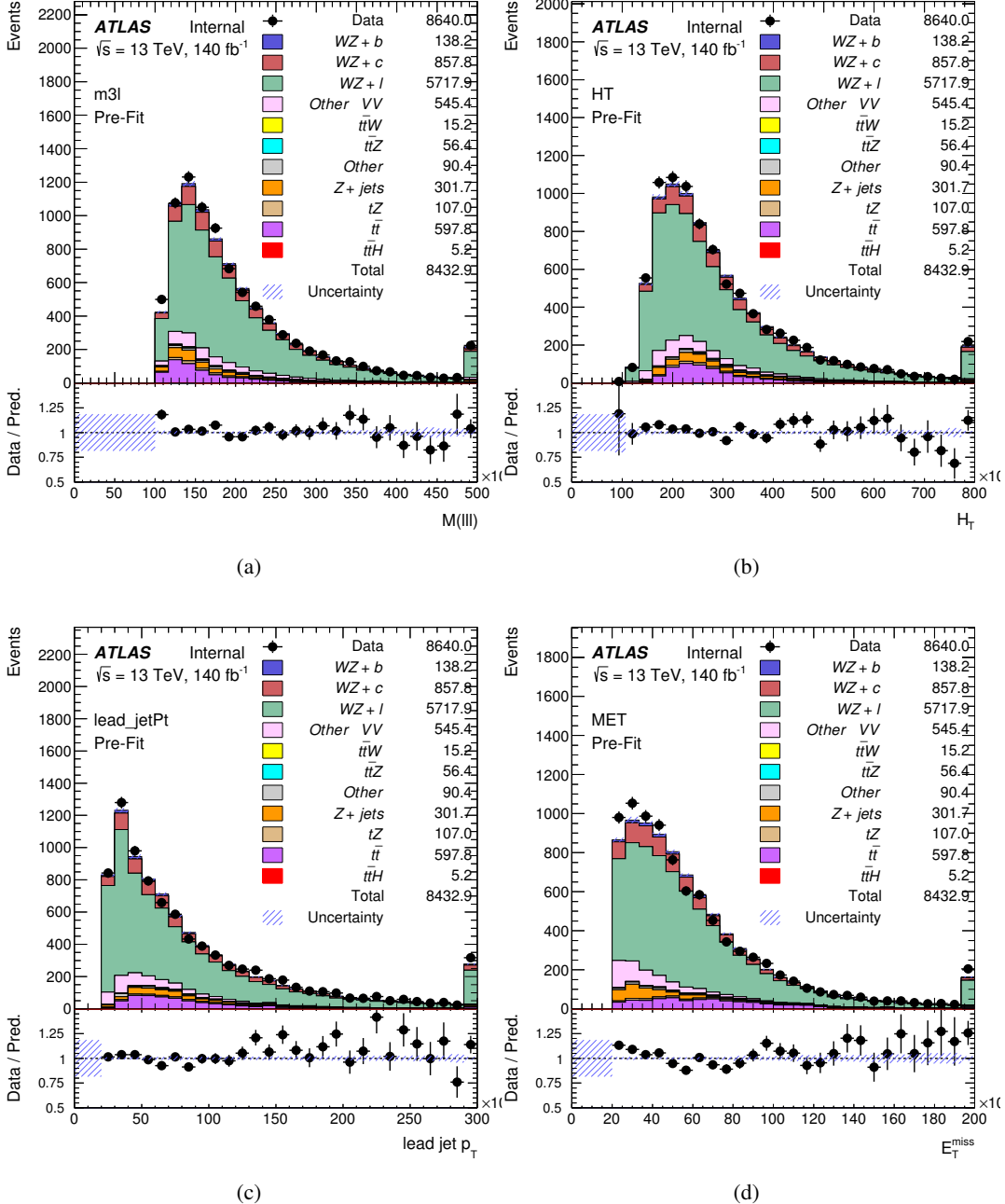


Figure 2: Comparisons between the data and MC distributions in the signal region for (a) the invariant mass of the three leptons, (b) the H_T of each event, (c) the p_T of the leading jet, (d) the missing transverse energy.

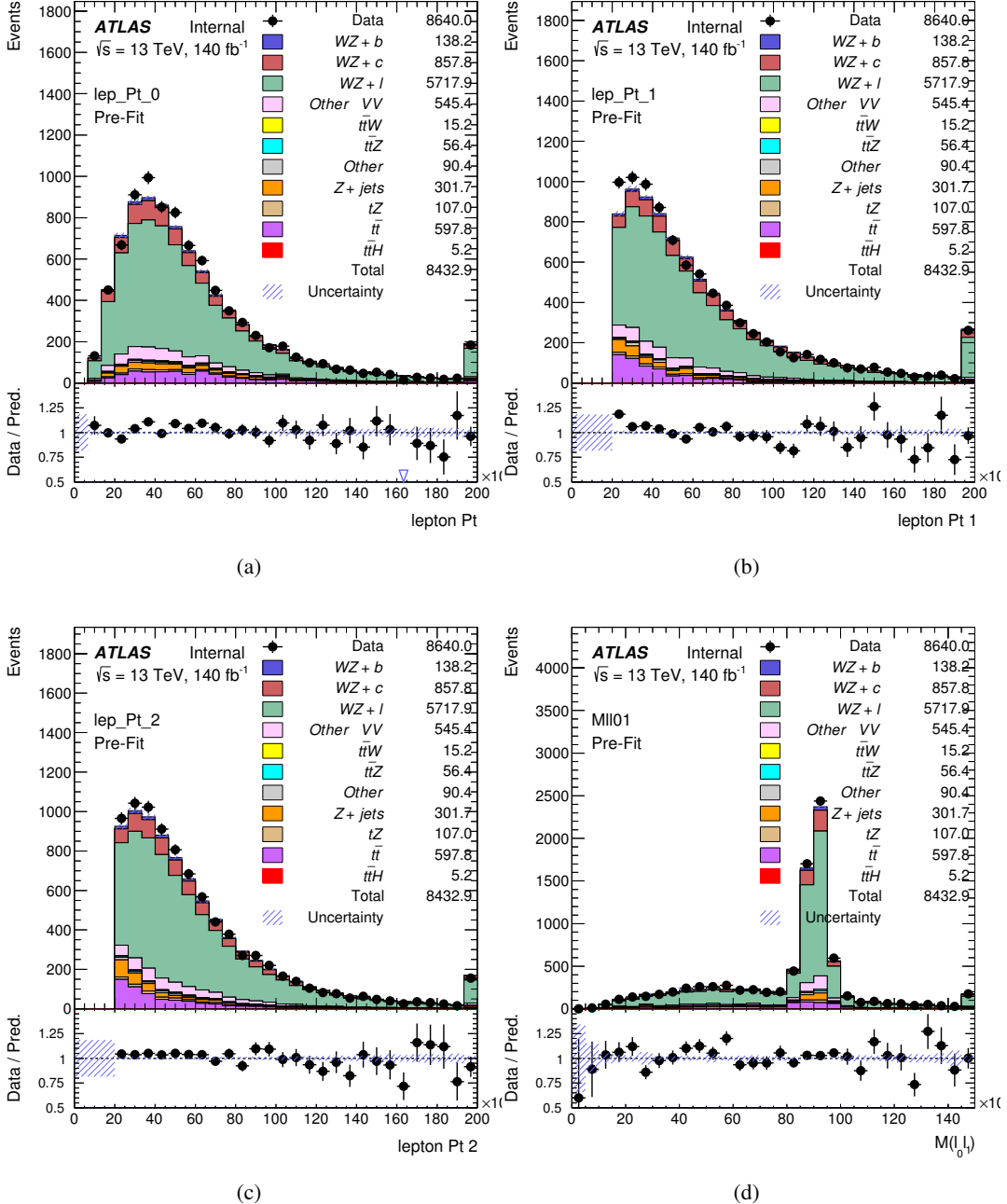


Figure 3: Comparisons between the data and MC distributions in the signal region for (a) the transverse momentum of the opposite sign lepton, (b) the transverse momentum of the same-sign lepton closest to the opposite sign lepton, (c) the p_T of the lepton furthest from the opposite sign lepton, (d) the invariant mass of lepton 0 and lepton 1.

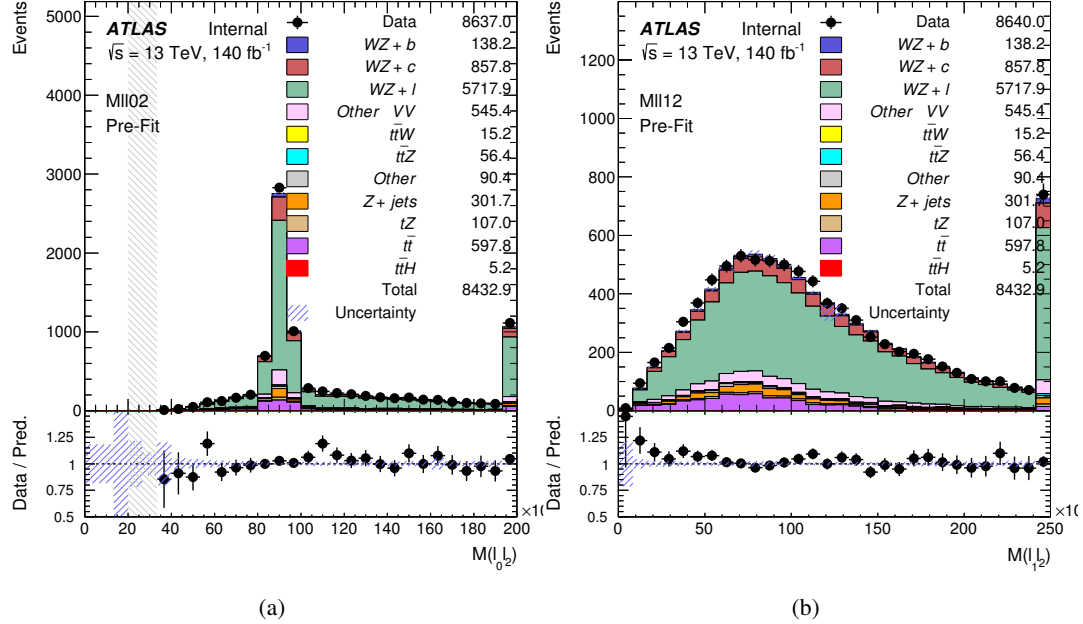


Figure 4: Comparisons between the data and MC distributions in the signal region for (a) the invariant mass of leptons 0 and 2, (b) the invariant mass of the pair of leptons 1 and 2

Figure 5: WZ Fit Region - Inclusive

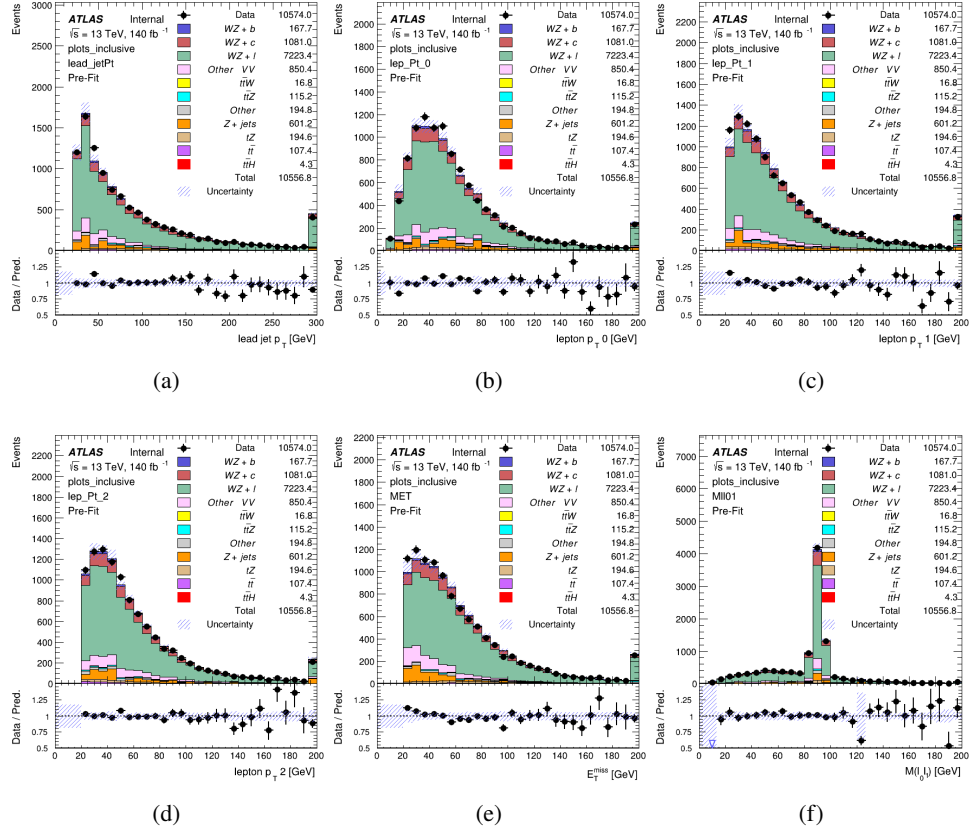


Figure 6: WZ Fit Region - 1j < 85% WP

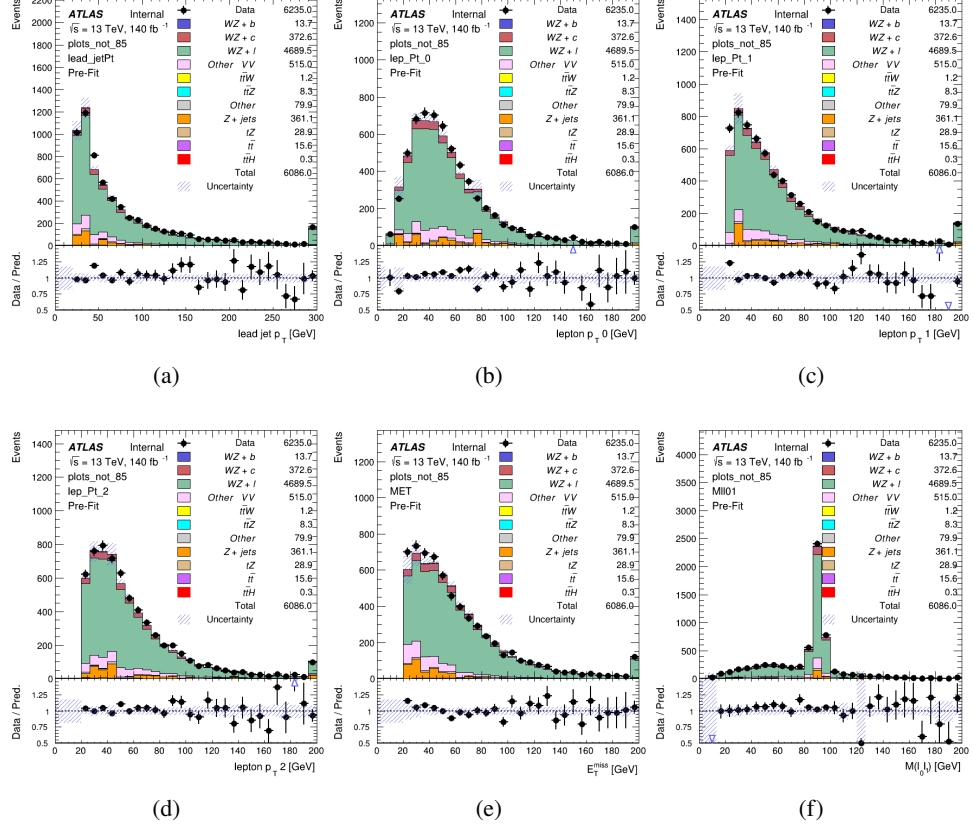


Figure 7: WZ Fit Region - 1j 77-85% WP

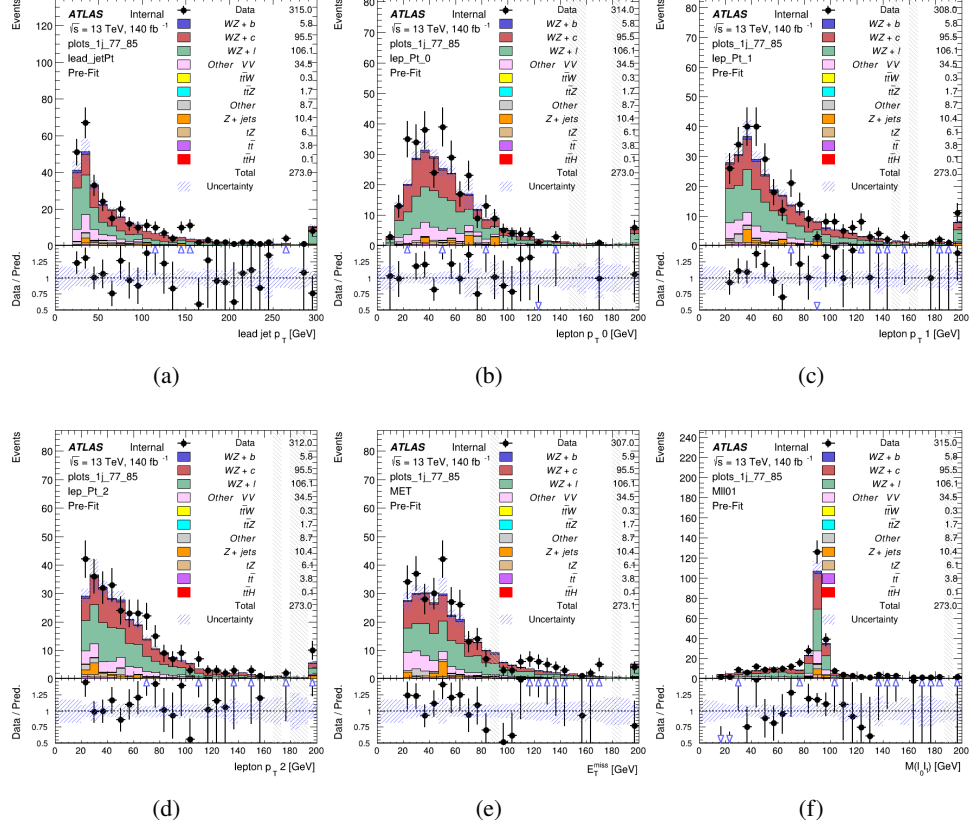


Figure 8: WZ Fit Region - 1j 70-77% WP

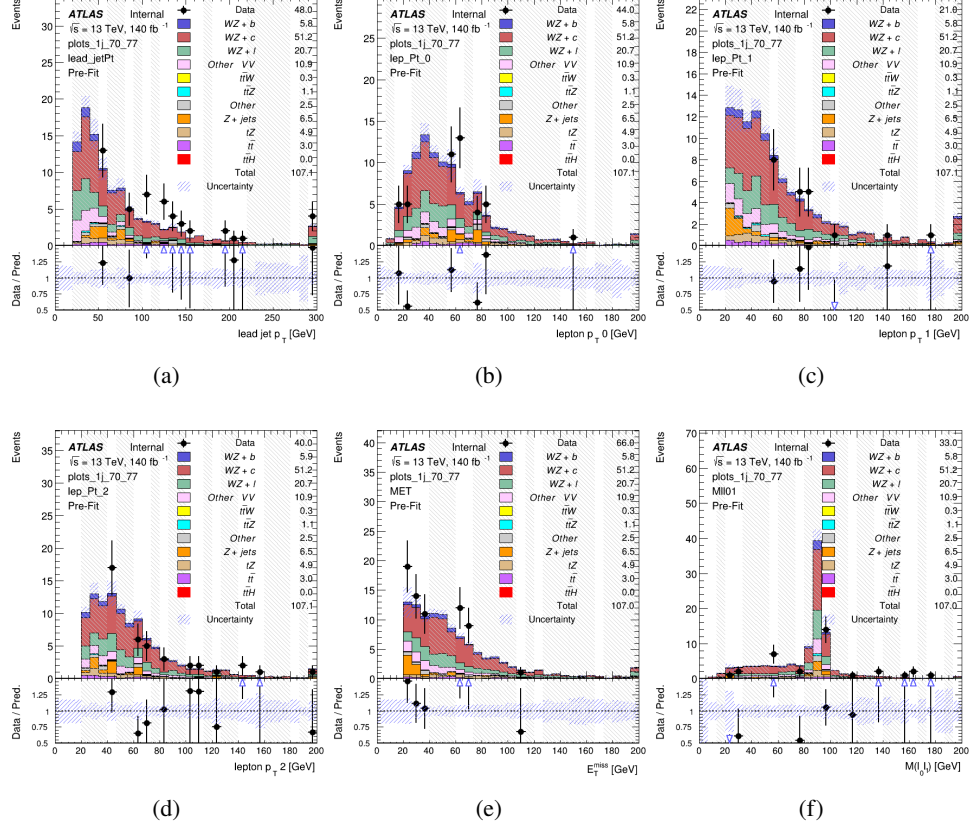


Figure 9: WZ Fit Region - 1j 60-70% WP

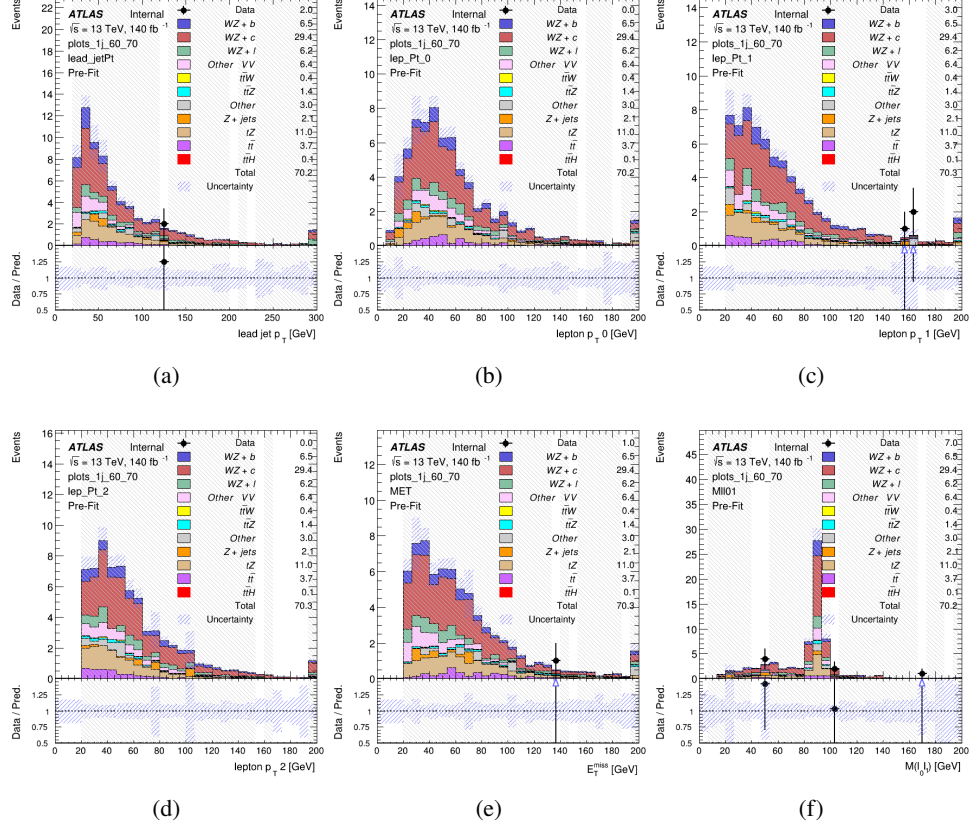


Figure 10: WZ Fit Region - 1j 60% WP

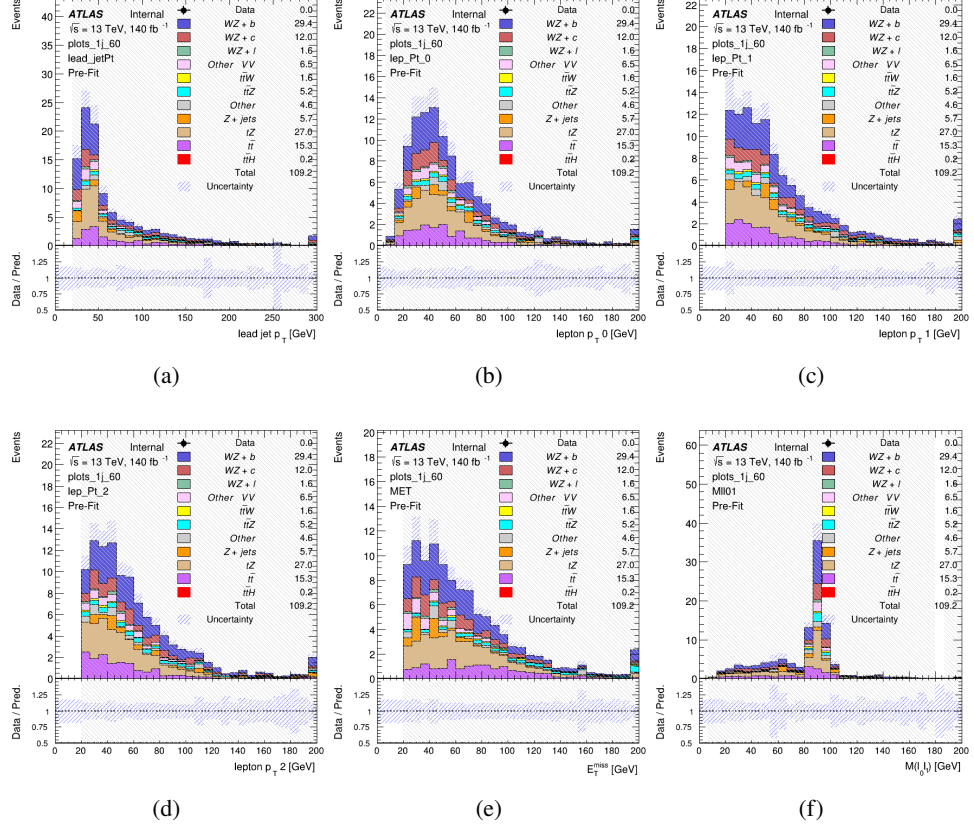


Figure 11: WZ Fit Region - tZ-CR

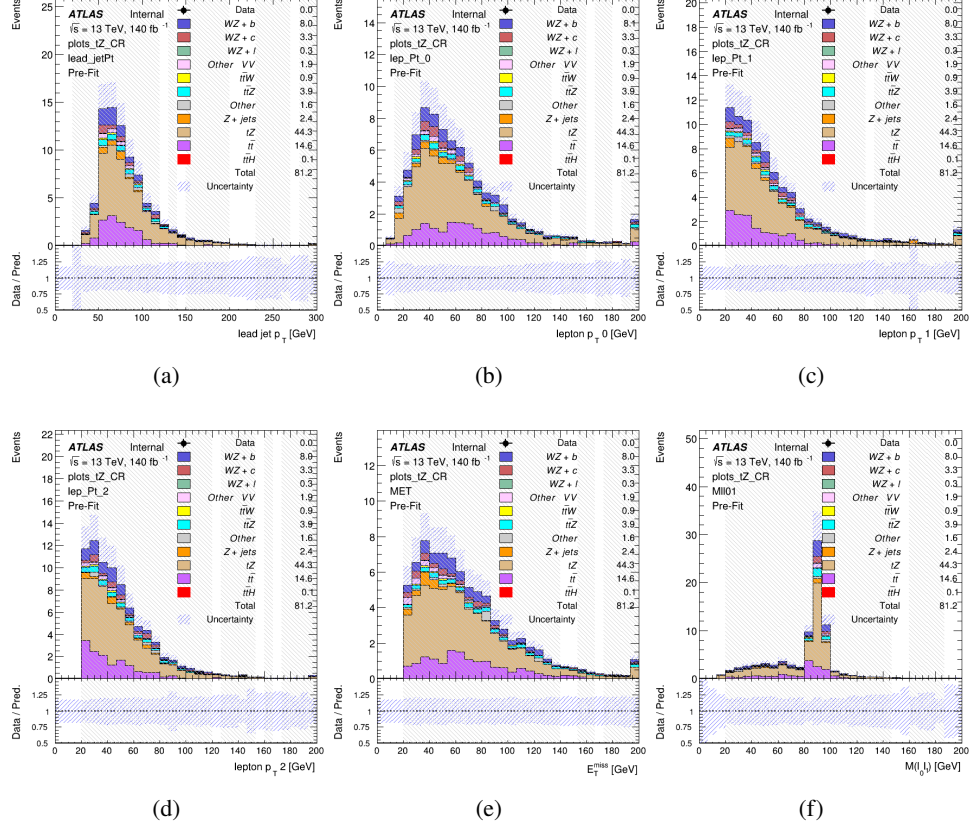


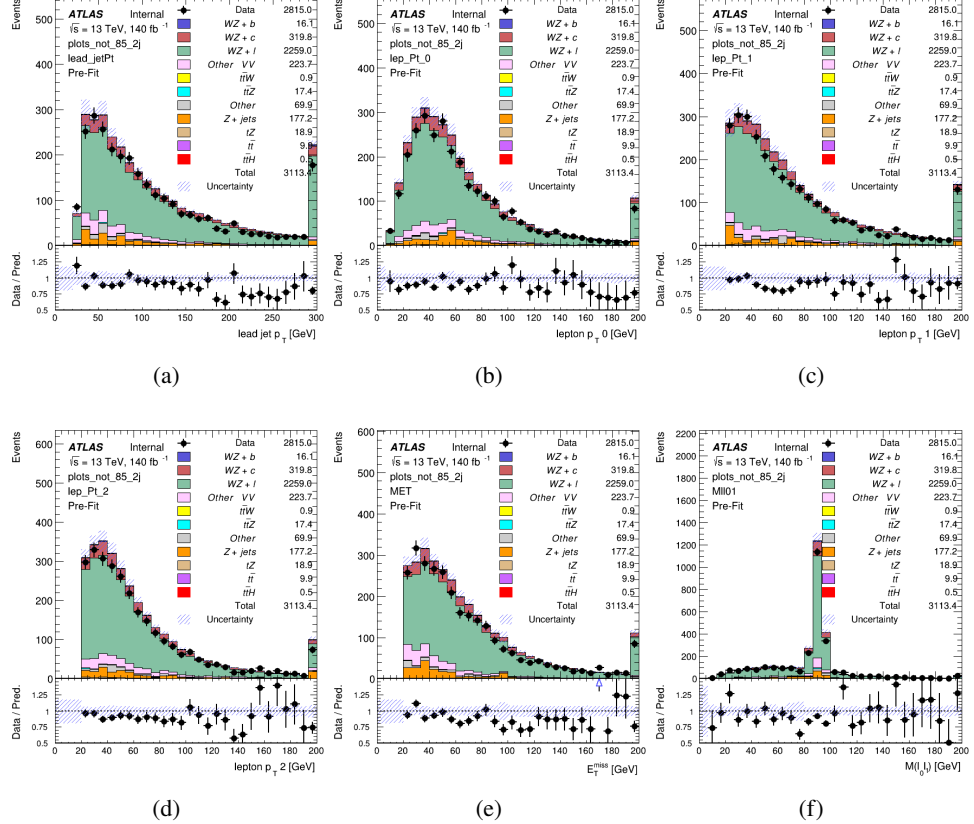
Figure 12: WZ Fit Region - $2j < 85\% \text{ WP}$ 

Figure 13: WZ Fit Region - 2j 77-85% WP

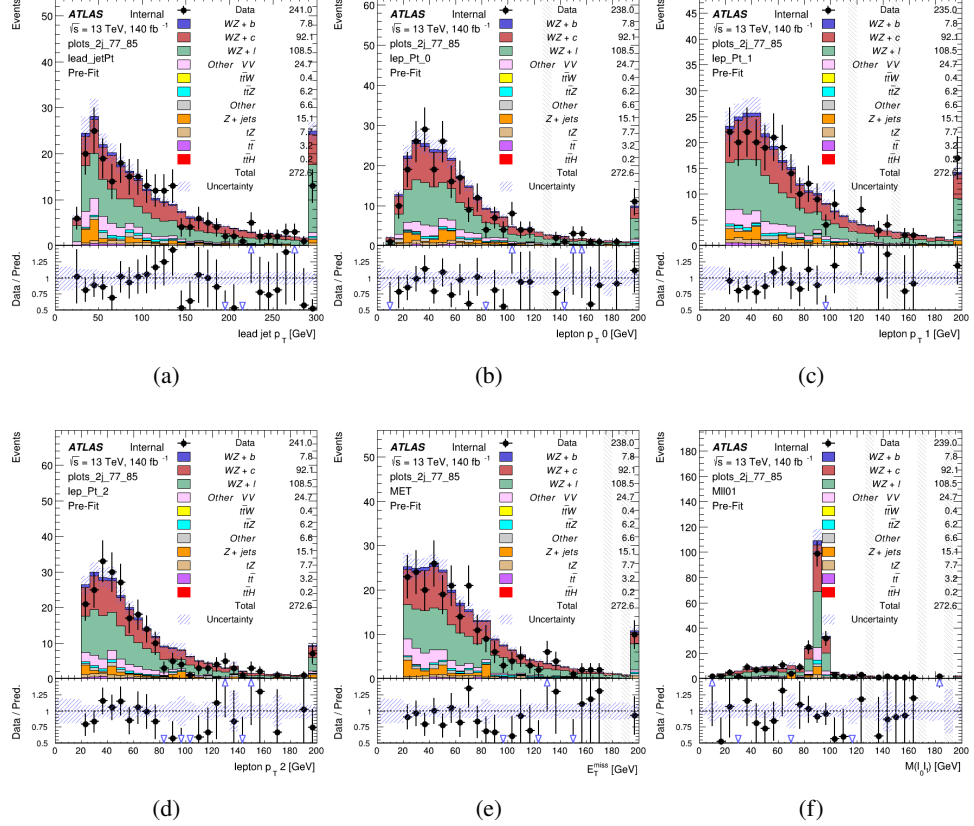


Figure 14: WZ Fit Region - 2j 70-77% WP

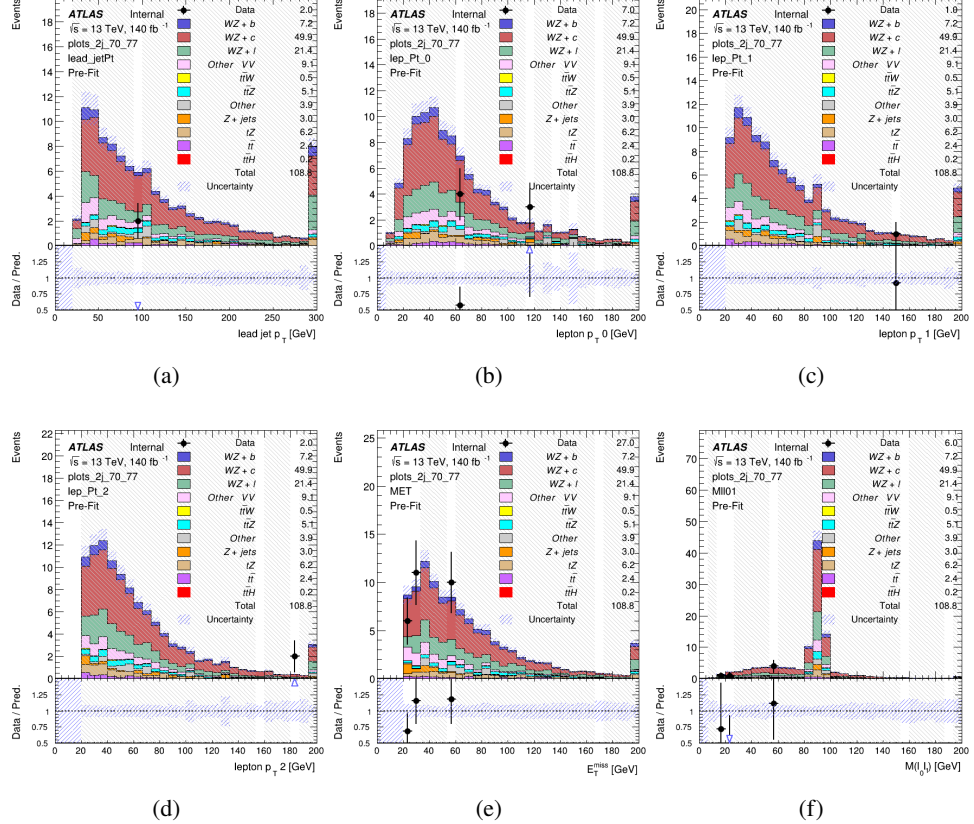


Figure 15: WZ Fit Region - 2j 60-70% WP

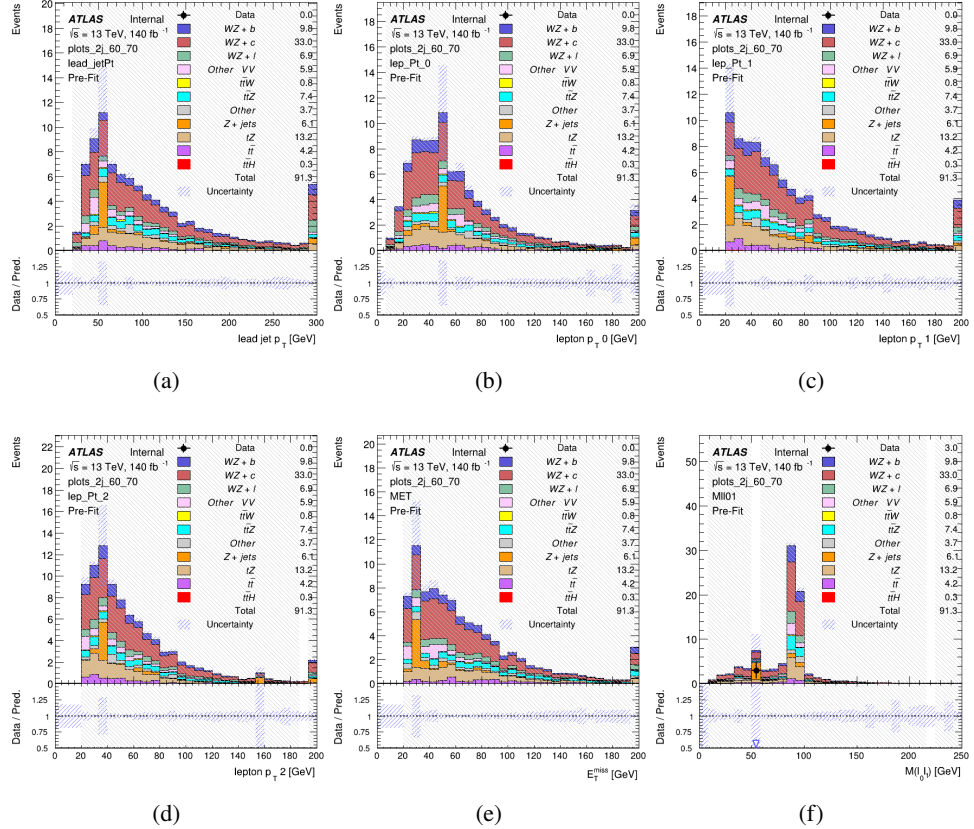
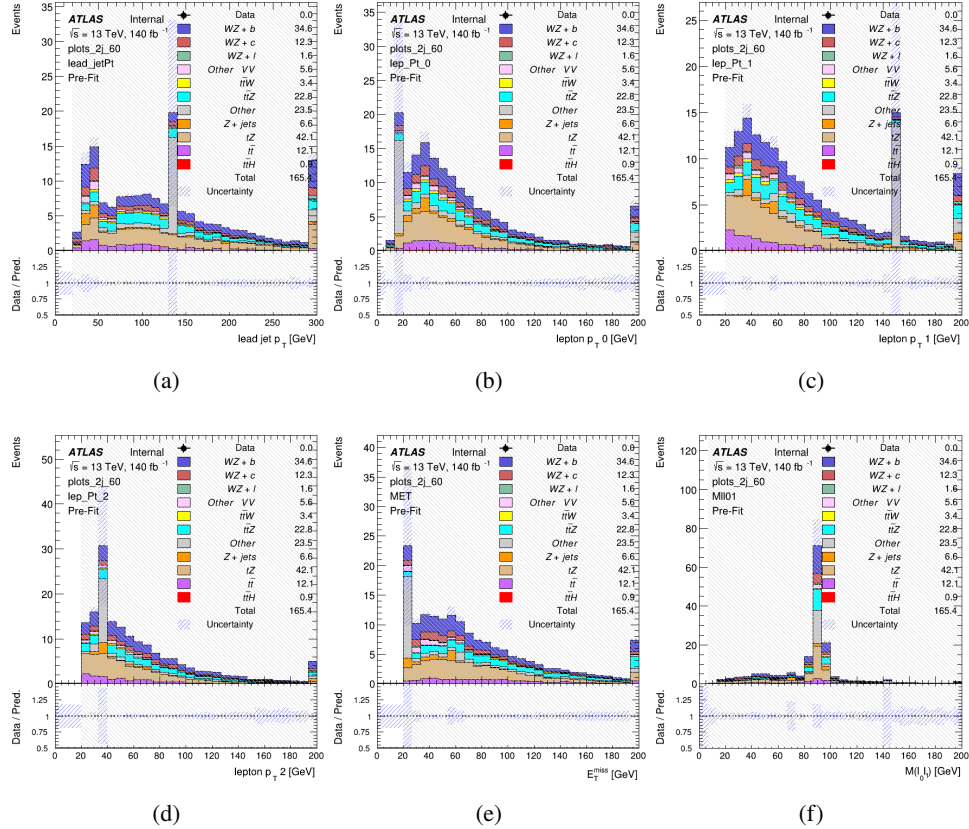


Figure 16: WZ Fit Region - 2j 60% WP



175 5.2 Non-Prompt Lepton Estimation

176 Two processes act as sources of non-prompt leptons appear in the analysis: $t\bar{t}$ and $Z+jet$
 177 production both produce two prompt leptons, and each contribute to the signal region when
 178 an additional non-prompt lepton appears in the event. The contribution of these processes is
 179 estimated with Monte Carlo simulations, which are validated using enriched validation regions.

180 5.2.1 $t\bar{t}$ Validation

181 $t\bar{t}$ events can produce two prompt leptons from the decay of each of the tops. These top decays
 182 produce two b-quarks, the decay of which can produce additional non-prompt leptons, which
 183 occasionally pass the selection of the signal region. In order to validate that the Monte Carlo
 184 accurately simulates this process accurately, the MC prediction in a non-prompt $t\bar{t}$ enriched
 185 validation region is compared to data.

186 The $t\bar{t}$ validation region is similar to the signal region - three leptons meeting the criteria
187 described in section 5 are required, and the requirements on E_T^{miss} remain the same. However,
188 the selection requiring a lepton pair form a Z-candidate are reversed. Events where the invariant
189 mass of any two opposite sign, same flavor leptons falls within 10 GeV of 91.2 GeV are rejected.
190 This ensures the $t\bar{t}$ validation region is orthogonal to the signal region.

191 Further, because the jet multiplicity of $t\bar{t}$ events tends to be higher than WZ, the number of jets
192 in each event is required to be greater than 1. As b-jets are almost invariably produced from top
193 decays, at least one b-tagged jet in each event is required.

194 Various kinematic plots of this region are shown below. The general agreement between data and
195 MC in each of these suggests that the non-prompt contribution of $t\bar{t}$ is well modeled by Monte
196 Carlo.

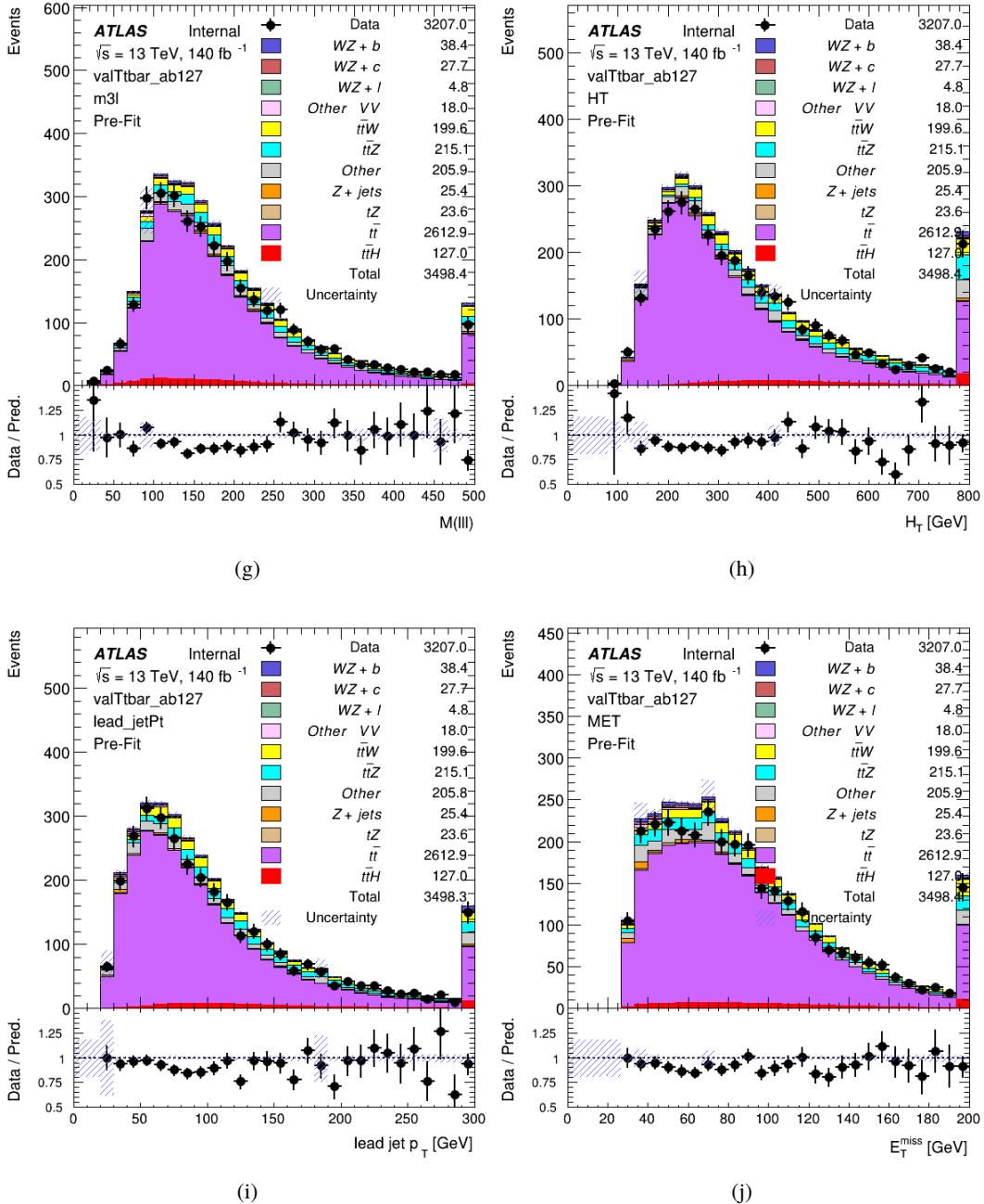


Figure 17: Comparisons between the data and MC distributions in the $t\bar{t}$ validation region for (a) the invariant mass of the three leptons, (b) the H_T of each event, (c) the p_T of the leading jet, (d) the missing transverse energy.

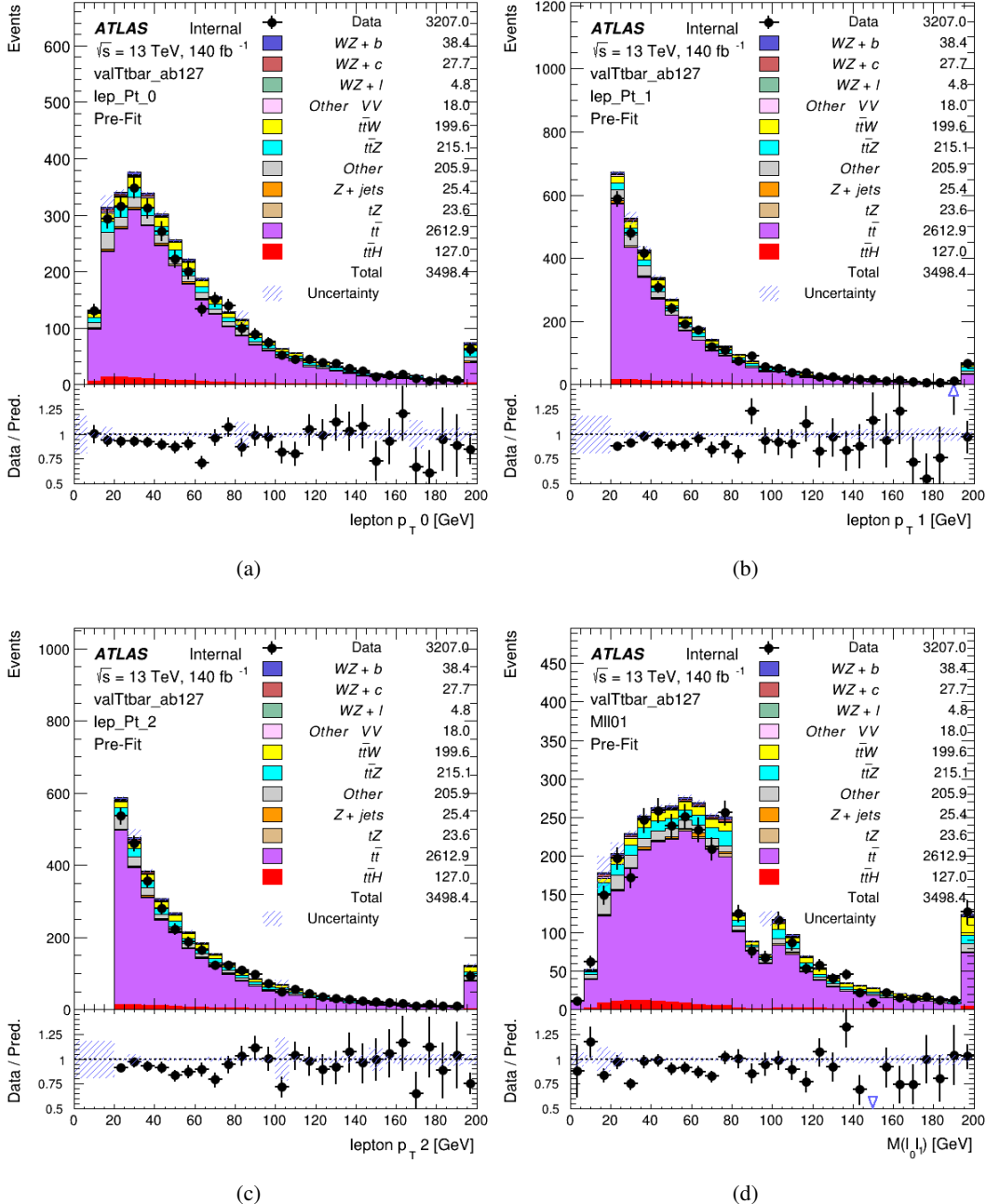


Figure 18: Comparisons between the data and MC distributions in the $t\bar{t}$ validation region for (a) the transverse momentum of the opposite sign lepton, (b) the transverse momentum of the same-sign lepton closest to the opposite sign lepton, (c) the p_T of the lepton furthest from the opposite sign lepton, (d) the invariant mass of lepton 0 and lepton 1.

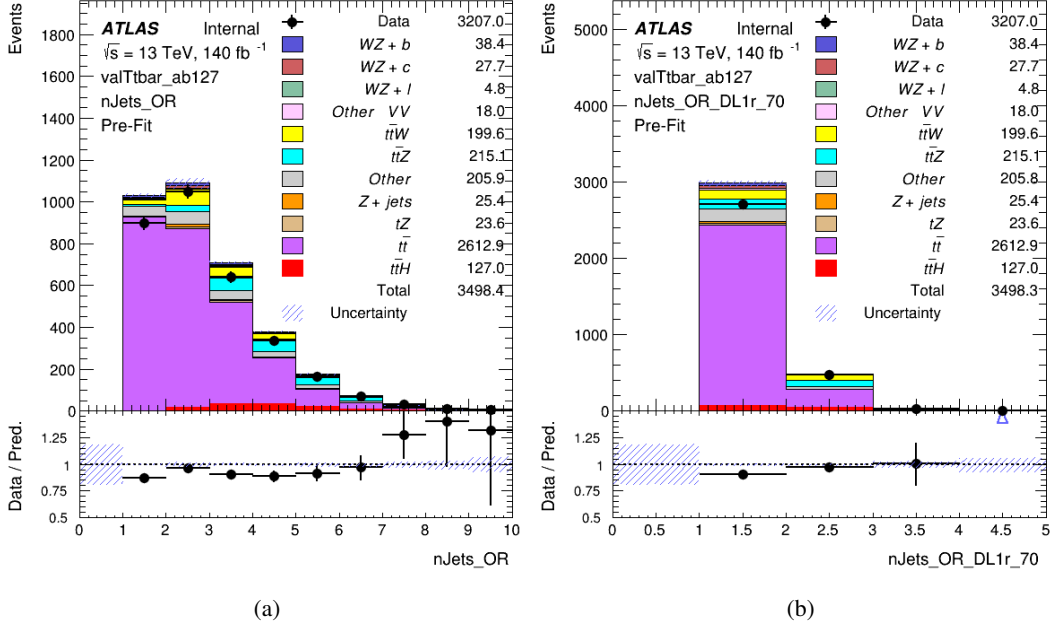


Figure 19: Comparisons between the data and MC distributions in the $t\bar{t}$ validation region for (a) the number of jets, (b) the number of b-tagged jets.

5.2.2 Z+jets Validation

Similar to $t\bar{t}$, a non-prompt Z +jets validation region is produced in order to validate the MC predictions. The lepton requirements remain the same as the signal region. Because no neutrinos are present for this process, the E_T^{miss} cut is reversed, requiring $E_T^{\text{miss}} < 30 \text{ GeV}$. This also ensures this validation region is orthogonal to the signal region. Further, the number of jets in each event is required to be greater than one.

Various kinematic plots of this region are shown below. The general agreement between data and MC in each of these suggests that the non-prompt contribution of Z +jets is well modeled by Monte Carlo.

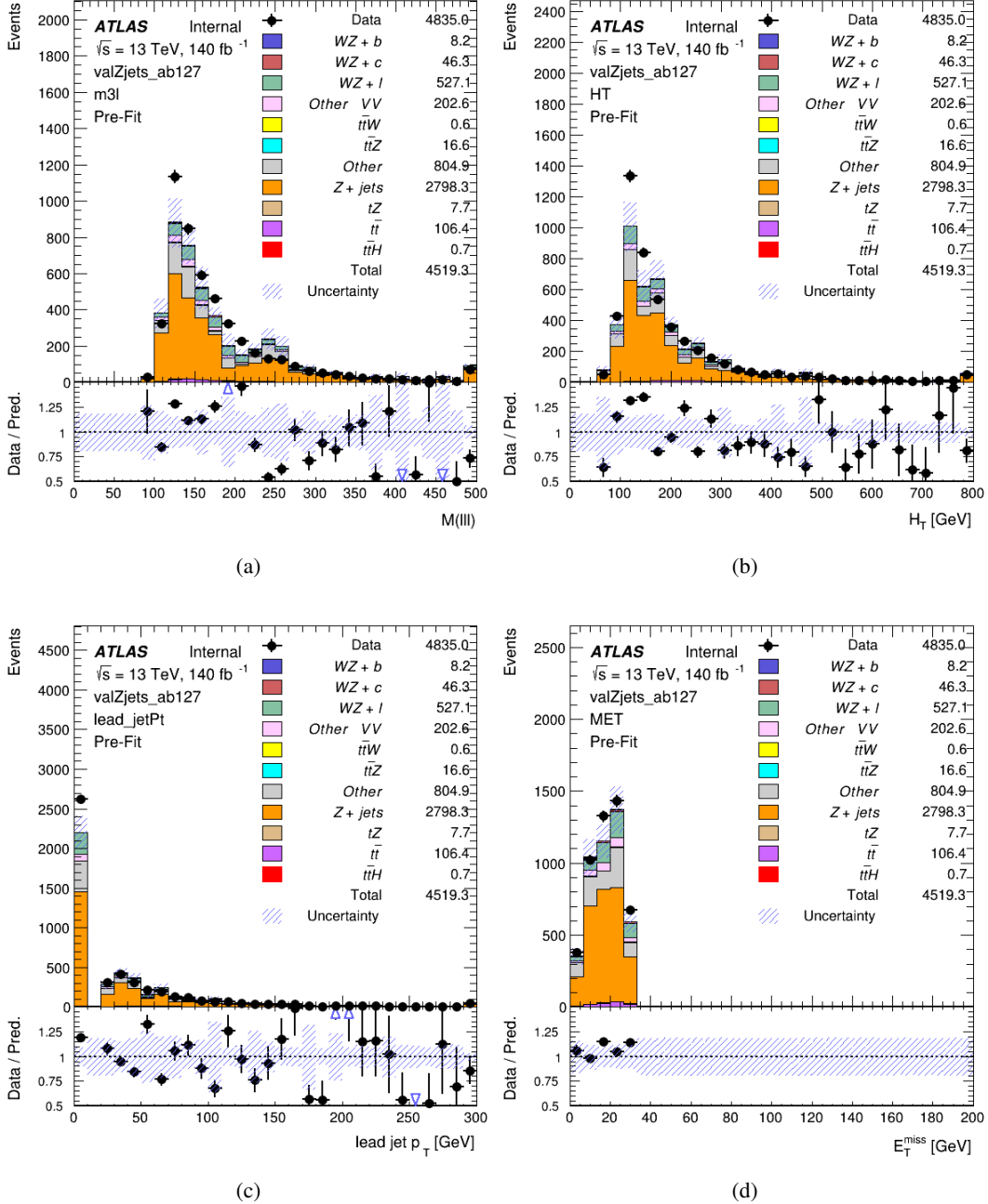


Figure 20: Comparisons between the data and MC distributions in the $t\bar{t}$ validation region for (a) the invariant mass of the three leptons, (b) the H_T of each event, (c) the p_T of the leading jet, (d) the missing transverse energy.

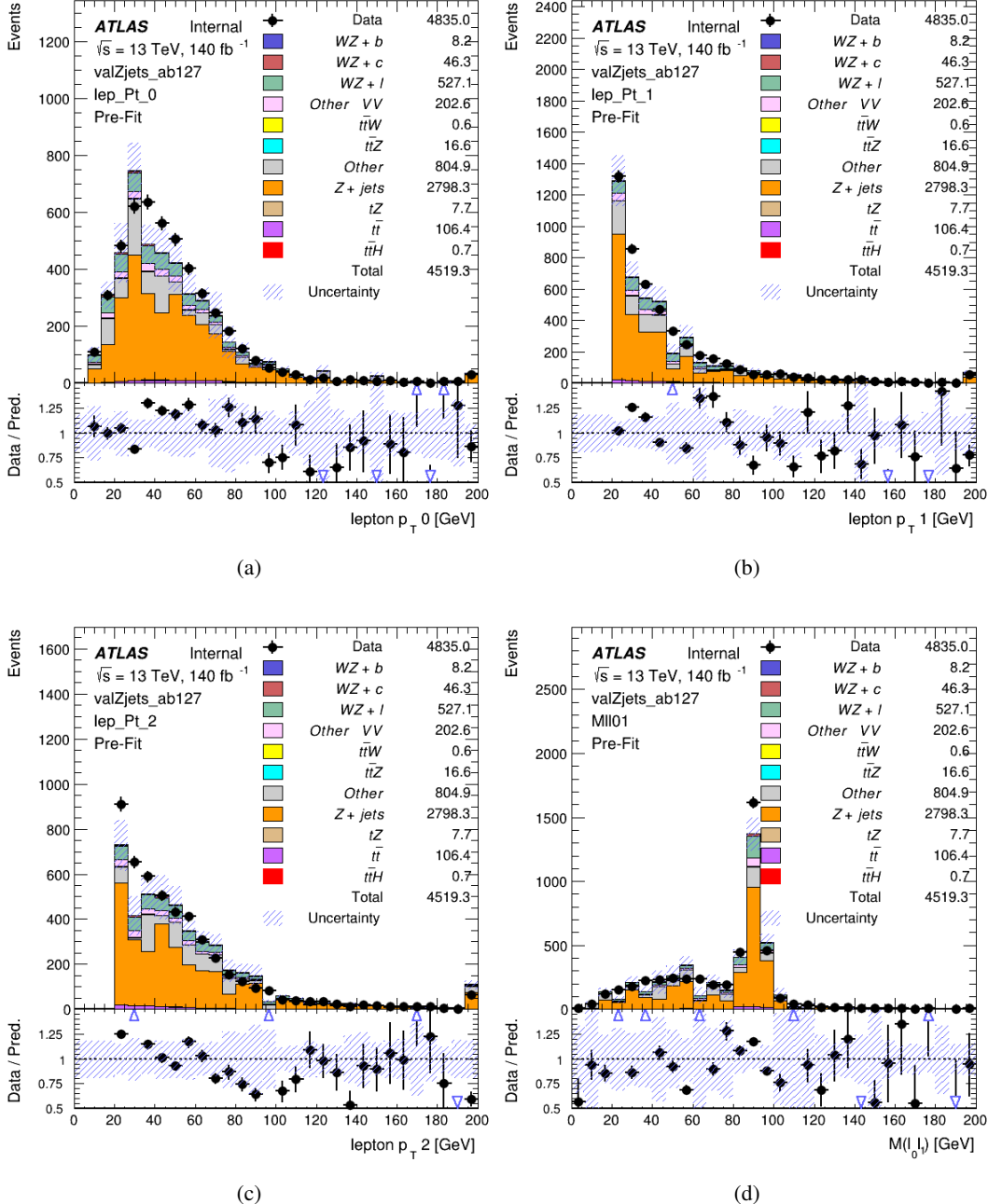


Figure 21: Comparisons between the data and MC distributions in the $Z + \text{jets}$ validation region for (a) the transverse momentum of the opposite sign lepton, (b) the transverse momentum of the same-sign lepton closest to the opposite sign lepton, (c) the p_T of the lepton furthest from the opposite sign lepton, (d) the invariant mass of lepton 0 and lepton 1.

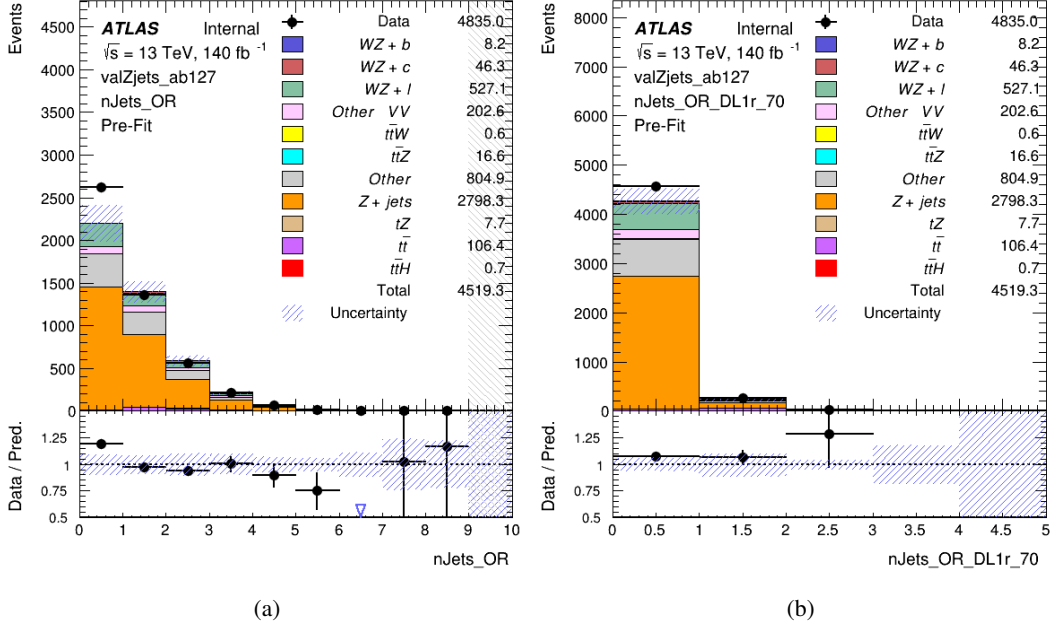


Figure 22: Comparisons between the data and MC distributions in the $Z + \text{jets}$ validation region for (a) the number of jets, (b) the number of b-tagged jets.

206 6 tZ Interference Studies and Separation Multivariate Analysis

207 Because it includes an on-shell Z boson as well as a b-jet and W from the top decay, tZ
 208 production represents an identical final state to $WZ + b$ -jet. This implies the possibility of matrix
 209 level interference between these two processes not accounted for in the Monte Carlo simulations,
 210 which consider the two processes independently. Truth level studies are performed in order to
 211 estimate the impact of these interference effects.

212 Because tZ produces a final state identical to signal, it represents a predominant background in
 213 the most signal enriched regions. Therefore, a boosted decision tree (BDT) algorithm is trained
 214 using TMVA [10] to separate $WZ + \text{heavy flavor}$ from tZ .

215 Separation between tZ and $WZ + \text{heavy flavor}$ is achieved in part by reconstructing the invariant
 216 mass of the top candidate, which clusters more closely to the top mass for tZ than $WZ + \text{heavy}$
 217 flavor.

218 The result of this BDT is used to create a tZ enriched region in the fit, reducing its impact on the
 219 measurement of $WZ + \text{heavy flavor}$.

220 **6.1 Interference Studies**

221 In order to estimate the matrix level interference effects between tZ and WZ + b-jet, two different
 222 sets of simulations are produced using MadGraph 5 [Madgraph] - one which simulates these
 223 two processes independently, and another where they are produced simultaneously, such that
 224 interference effects are present. These two sets of samples are then compared, and the difference
 225 between them can be taken to represent any interference effects.

226 MadGraph simulations of 10,000 tZ and 10,000 WZ + b-jet events are produced, along with
 227 20,000 events where both are present, in the fiducial region where three leptons and at least one
 228 jet are produced.

229 The kinematics of these samples are shown below:

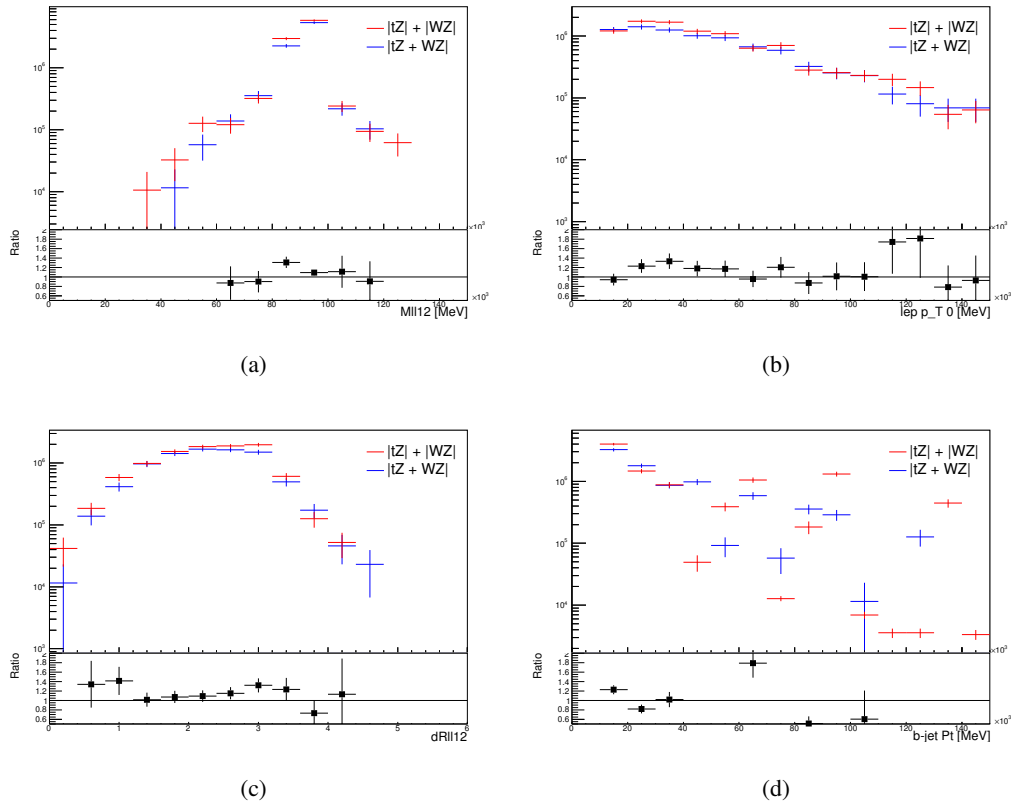


Figure 23: Comparisons between (a) the invariant mass of the Z-candidate, (b) the p_T of the leading lepton, (c) $\Delta(R)$ of the two leptons that form the Z-candidate, and (d) the p_T of the b-jet, for WZ and tZ events generated with interference effects (blue) and without interference effects (red).

230 **6.2 Top Mass Reconstruction**

231 The reconstruction of the top mass follows the procedure described in detail in section 6.1 of
 232 [11]. The mass of the top quark candidate is reconstructed from the jet, the lepton not included
 233 in the Z-candidate, and a reconstructed neutrino. Since the selection requires exactly one jet in
 234 the event, there is only possible b-jet candidate.

235 The neutrino from the W decay is expected to be the only source of E_T^{miss} . Therefore, the E_T
 236 and ϕ of the neutrino are taken from the E_T^{miss} measurement. This leaves the z-component of
 237 the neutrino momentum, $p_{\nu z}$ as the only unknown.

238 This unknown is solved for by taking the combined invariant mass of the lepton and neutrino to
 239 give the invariant mass of the W boson:

$$240 \quad (p_l + p_\nu)^2 = m_W^2$$

241 Expanding this out into components, this equation gives:

$$242 \quad \sqrt{p_{T\nu}^2 + p_{z\nu}^2} E_l = \frac{m_W^2 - m_l^2}{2} + p_{T\nu}(p_{lx}\cos\phi_\nu + p_{ly}\sin\phi_\nu) + p_{lz}p_{\nu z}$$

243 This equation gives two solutions for $p_{\nu z}$. For cases where only one of these solutions is real,
 244 that is taken as the value of $p_{\nu z}$. For instances with two real solutions, the one which is shown
 245 to be correct in the largest fraction of simulations is taken. For cases when no real solution is
 246 found, often because of detector effects, the value of E_T^{miss} is varied in decreasing increments of
 247 100 MeV until a real solution is found.

248 The reconstructed top mass distribution for tZ and WZ + b can be seen in figure ??.

249 **6.3 tZ BDT**

250 The following kinematic variables are used as inputs in order to distinguish between these two
 251 processes:

- 252 • The invariant mass of the reconstructed top candidate
- 253 • p_T of each of the leptons
- 254 • E_T^{miss}
- 255 • Distance between each combination of leptons, $\Delta R(ll)$
- 256 • Distance between each lepton and the jet, $\Delta R(lj)$

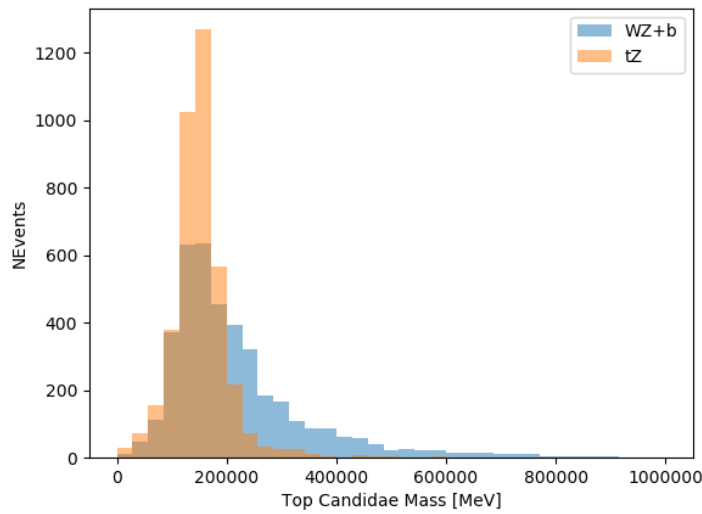


Figure 24: Reconstructed top mass distributions for tZ and WZ + b, measured in MeV.

257 The training samples included only events meeting the requirements of the 1-jet, >60% region,
 258 i.e. passing all the selection described in section 5 and having exactly one jet which passes the
 259 tightest (60%) DL1r working point.

260 The distributions of these features for both signal and background is shown in figure ??.

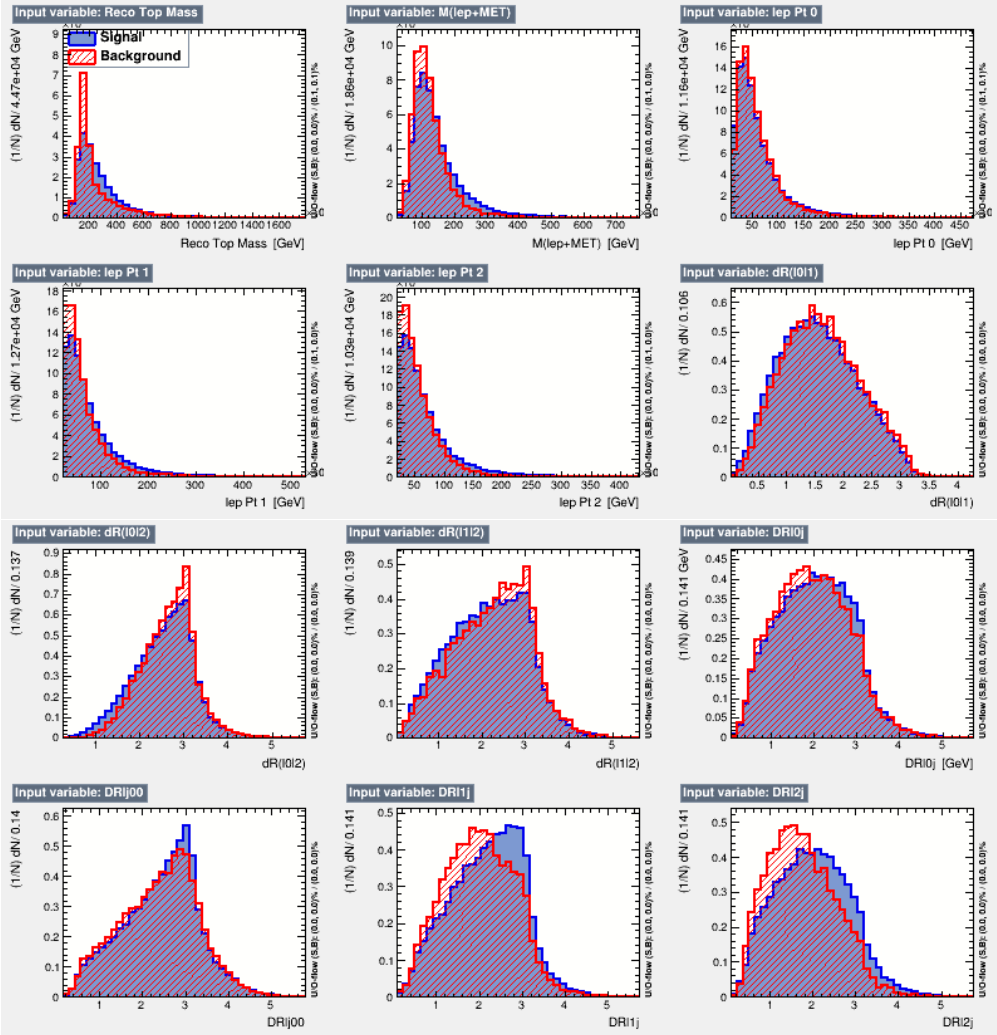


Figure 25: Distribution of input features of the BDT for signal (WZ) and background (tZ).

261 A sample of 20,000 background (tZ) and signal (WZ+b) Monte Carlo events are used to train
 262 the BDT. And additional 5,000 events are reserved for testing the model, in order to prevent
 263 over-fitting. A total of 750 decision trees with a maximum depth of 6 branches are used to build
 264 the model. These parameters are chosen empirically, by training several models with different
 265 parameters and selecting the one that gave the best separation for the test sample.

266 The results of the BDT training are shown in figure ???. The output scores for both signal and
 267 background events is shown on the left. The right shows the receiving operating characteristic
 268 (ROC) curve that results from the MVA. The ROC curve represents the background rejection
 269 as a function of signal efficiency, where each point on the curve represents a different response
 270 score. The ROC curve of the BDT is compared to the performance of using an optimal set of flat
 271 selections on the same set of input variables.

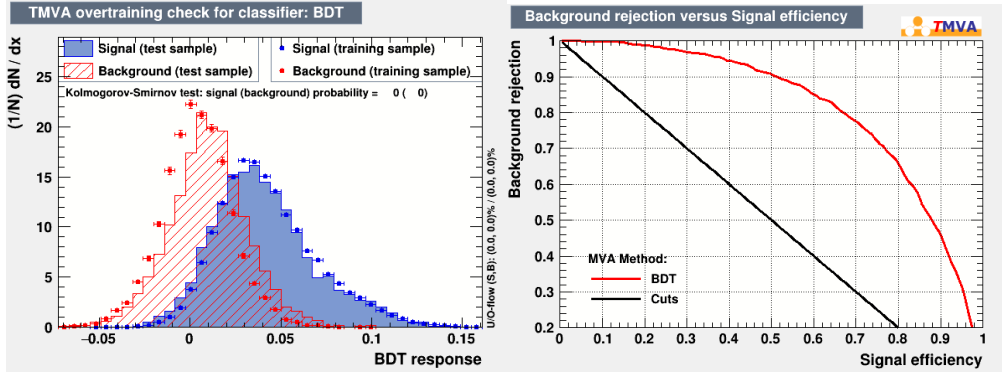


Figure 26: Distribution of the BDT response for signal and background events on the left, the ROC curve for the BDT on the right.

272 These results suggest that some amount of separation can be achieved between these two pro-
273 cesses, with a high BDT score selecting a set of events that is pure in $WZ + b$. Further, the ROC
274 curve demonstrates the BDT performs significantly better than a flat selection.

275 7 Signal Region Definitions

276 The regions used in the fit are summarized in table ??.

Table 9: A list of the regions used in the fit and the selection used for each.

Region	Selection
1j, <85%	$N_{\text{jets}} = 1$, jet DL1r score < 85% WP
1j, 85%-77%	$N_{\text{jets}} = 1$, 85% < jet DL1r score < 77% WP
1j, 77%-70%	$N_{\text{jets}} = 1$, 77% < jet DL1r score < 70% WP
1j, 70%-60%	$N_{\text{jets}} = 1$, 70% < jet DL1r score < 60% WP
1j, >60%	$N_{\text{jets}} = 1$, jet DL1r score > 85% WP, tZ BDT score > 0.03
1j tZ CR	$N_{\text{jets}} = 1$, jet DL1r > 85% WP, tZ BDT score < 0.03
2j, <85%	$N_{\text{jets}} = 2$, jet DL1r score < 85% WP
2j, 85%-77%	$N_{\text{jets}} = 2$, 85% WP < jet DL1r score < 77% WP
2j, 77%-70%	$N_{\text{jets}} = 2$, 77% WP < jet DL1r score < 70% WP
2j, 70%-60%	$N_{\text{jets}} = 2$, 70% < jet DL1r score < 60% WP
2j, >60%	$N_{\text{jets}} = 2$, jet DL1r score > 85% WP, tZ BDT score > 0.03
2j tZ CR	$N_{\text{jets}} = 2$, jet DL1r score > 85% WP, tZ BDT score < 0.03

277 The working points discussed in section 4.4 are used to separate events into fit regions based on
278 the highest working point reached by a jet in each event. Because the background composition
279 differs significantly based on the number of b-jets, events are further subdivided into 1 jet and 2
280 jet regions in order to minimize the impact of background uncertainties.

281 An additional tZ control region is created based on the BDT described in section ?? . The region
 282 with 1-jet passing the 60% working point is split in two - a signal enriched region of events with
 283 a BDT score greater than 0.03, and a tZ control region including events with less than 0.03. This
 284 cutoff is arrived at by performing an Asimov fit with a variety of cutoffs, and selecting the value
 285 that produces the highest significance for the measurement of WZ + b.

286 8 Systematic Uncertainties

287 The systematic uncertainties that are considered are summarized in table ?? . These are imple-
 288 mented in the fit either as a normalization factors or as a shape variation or both in the signal
 289 and background estimations. The numerical impact of each of these uncertainties is outlined in
 290 section ?? .

Table 10: Sources of systematic uncertainty considered in the analysis.

Systematic uncertainty	Components
Luminosity	1
Pileup reweighting	1
Physics Objects	
Electron	6
Muon	15
Jet energy scale and resolution	28
Jet vertex fraction	1
Jet flavor tagging	131
E_T^{miss}	3
Total (Experimental)	186
Background Modeling	
Cross section	24
Renormalization and factorization scales	10
Parton shower and hadronization model	2
Shower tune	4
Total (Signal and background modeling)	40
Total (Overall)	226

291 The uncertainty in the combined integrated luminosity is derived from a calibration of the
 292 luminosity scale performed in August 2015 and May 2016 [12].

293 The experimental uncertainties are related to the reconstruction and identification of light leptons
 294 and b-tagging of jets, and to the reconstruction of E_T^{miss} . The sources which contribute to the
 295 uncertainty in the jet energy scale [13] are decomposed into uncorrelated components and treated
 296 as independent sources in the analysis.

297 The uncertainties in the b-tagging efficiencies measured in dedicated calibration analyses [14] are
 298 also decomposed into uncorrelated components. The large number of components for b-tagging
 299 is due to the calibration of the distribution of the MVA discriminant.

300 The systematic uncertainties associated with the signal and background processes are accounted
 301 for by varying the cross-section of each process within its uncertainty.

302 The full list of systematic uncertainties considered in the analysis is summarized in tables ??, ??
 303 and ??.

304

Experimental Systematics on Leptons and E_T^{miss}			
Type	Description	Systematics Name	Application
Trigger			
Scale Factors	Trigger Efficiency	lepSFTrigTight_MU(EL)_SF_Trigger_STAT(SYST)	Event Weight
Muons			
Efficiencies	Reconstruction and Identification	lepSFObjTight_MU_SF_ID_STAT(SYST)	Event Weight
	Isolation	lepSFObjTight_MU_SF_Isol_STAT(SYST)	Event Weight
	Track To Vertex Association	lepSFObjTight_MU_SF_TTVA_STAT(SYST)	Event Weight
	p_T Scale	MUONS_SCALE	p_T Correction
Resolution	Inner Detector Energy Resolution	MUONS_ID	p_T Correction
	Muon Spectrometer	MUONS_MS	p_T Correction
	Energy Resolution		
Electrons			
Efficiencies	Reconstruction	lepSFObjTight_EL_SF_ID	Event Weight
	Identification	lepSFObjTight_EL_SF_Reco	Event Weight
	Isolation	lepSFObjTight_EL_SF_Isol	Event Weight
Scale Factor	Energy Scale	EG_SCALE_ALL	Energy Correction
Resolution	Energy Resolution	EG_RESOLUTION_ALL	Energy Correction
E_T^{miss}			
Soft Tracks Terms	Resolution	MET_SoftTrk_ResoPerp	p_T Correction
	Resolution	MET_SoftTrk_ResoPara	p_T Correction
	Scale	MET_SoftTrk_ScaleUp	p_T Correction
	Scale	MET_SoftTrk_ScaleDown	p_T Correction

Table 11: Summary of experimental systematics considered for leptons and E_T^{miss} . Includes type, description, name of systematic as used in the fit, and mode of application. The mode of application indicates the systematic evaluation, e.g. as an overall event re-weighting (Event Weight) or rescaling (p_T Correction).

Experimental Systematics on Jets			
Type	Origin	Systematics Name	Application
Jet Vertex Tagger		JVT	Event Weight
Energy Scale	Calibration Method	JET_21NP_ JET_EffectiveNP_1-19	p_T Correction p_T Correction
	η inter-calibration	JET_EtaIntercalibration_Modelling JET_EtaIntercalibration_NonClosure JET_EtaIntercalibration_TotalStat	p_T Correction p_T Correction p_T Correction
	High p_T jets	JET_SingleParticle_HighPt	p_T Correction
	Pile-Up	JET_Pileup_OffsetNPV JET_Pileup_OffsetMu JET_Pileup_PtTerm JET_Pileup_RhoTopology	p_T Correction p_T Correction p_T Correction p_T Correction
	Non Closure	JET_PunchThrough_MC15	p_T Correction
	Flavour	JET_Flavor_Response JET_BJES_Response JET_Flavor_Composition	p_T Correction p_T Correction p_T Correction
Resolution		JET_JER_SINGLE_NP	Event Weight

Table 12: Jet systematics take into account effects of jets calibration method, η inter-calibration, high p_T jets, pile-up, and flavor response. They are all diagonalised into effective parameters.

Experimental Systematics on b-tagging		
Type	Origin	Systematic Name
Scale Factors	DL1r b-tagger efficiency on b originated jets in bins of η	DL1r_Continuous_EventWeight_B0-29
	DL1r b-tagger efficiency on c originated jets in bins of η	DL1r_Continuous_EventWeight_C0-19
	DL1r b-tagger efficiency on light flavoured originated jets in bins of η and p_T	DL1r_Continuous_EventWeight_Light0-79
	DL1r b-tagger extrapolation efficiency	DL1r_Continuous_EventWeight_extrapolation DL1r_Continuous_EventWeight_extrapolation_from_charm

Table 13: Summary of experimental systematics to be included for b-tagging of jets in the analysis, using the continuous DL1r tagging algorithm. All of the b-tagging related systematics are applied as event weights. From left: type, description, and the name of systematic used in the fit.

9 Results

- 305 9 Results
- 306 A maximum-likelihood fit is performed simultaneously over these nine regions in order to extract
 307 the best-fit value of the WZ + b-jet and WZ + charm jet contributions. The WZ + b, WZ + charm
 308 and WZ + light contributions are allowed to float, with the remaining background contributions
 309 are held fixed. **The current fit strategy treats the WZ + b-jet contribution as the parameter**
 310 **of interest, with the normalization of the WZ + charm and the WZ + light contributions**
 311 **taken as systematic uncertainties. This could however be adjusted, depending on whether**
 312 **it is decided the goal of the analysis should be to measure WZ+b specifically or WZ + heavy**
 313 **flavor overall.** The result of the fit is used to extract the cross-section of WZ + heavy-flavor
 314 production.
- 315 A maximum likelihood fit to data is performed simultaneously in the eight regions described
 316 in section ???. The parameters μ_{WZ+b} , $\mu_{WZ+charm}$, $\mu_{WZ+light}$, where $\mu = \sigma_{\text{observed}}/\sigma_{\text{SM}}$, are
 317 extracted from the fit.
- 318 **The results of the fit are currently blinded.** The post-fit yields in each region are summarized
 319 in figure ???.
- 320 A post-fit summary plot of the fitted regions is shown in figure ???:

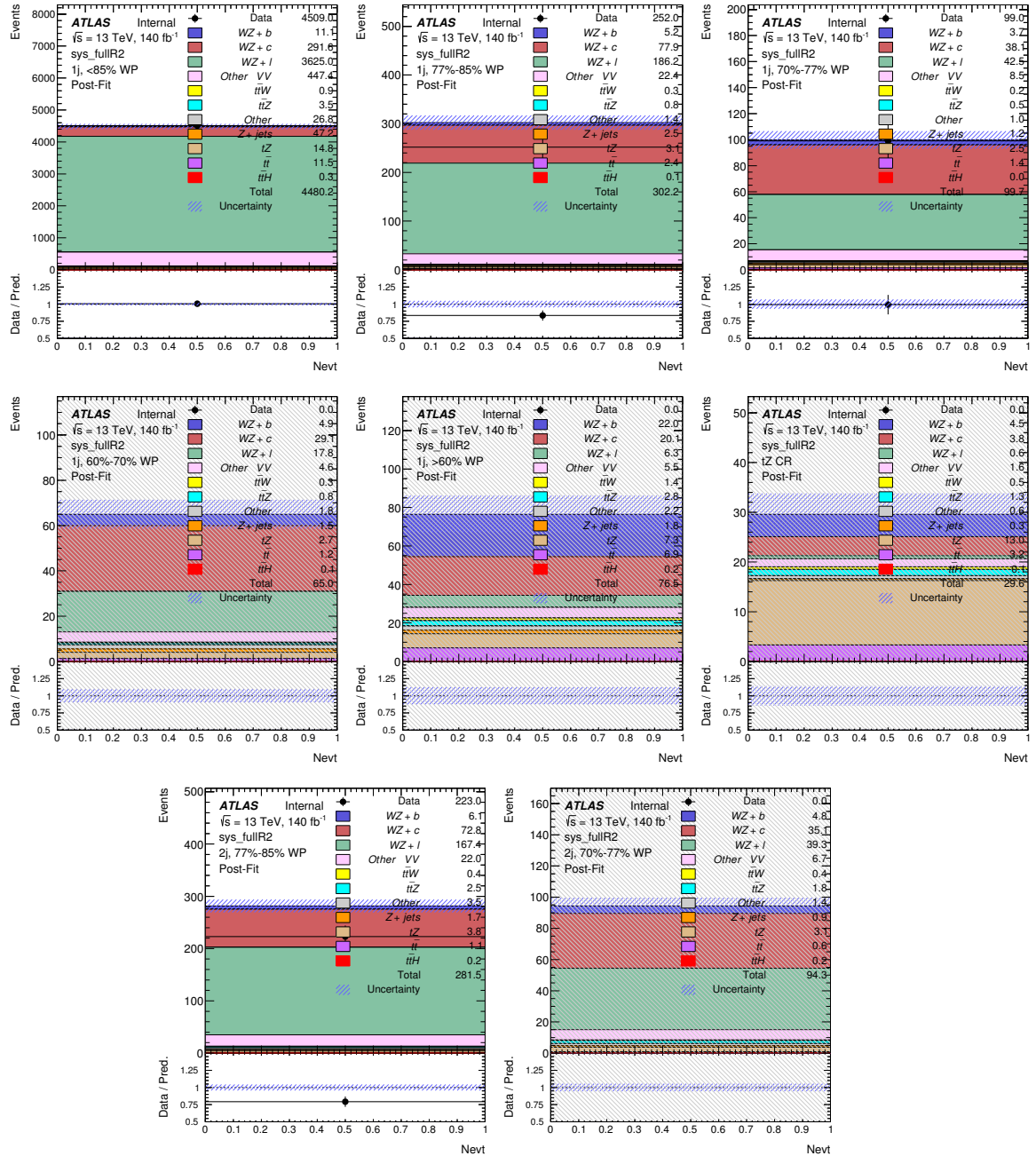


Figure 27: Data/MC results in each of the regions after the fit has been performed.

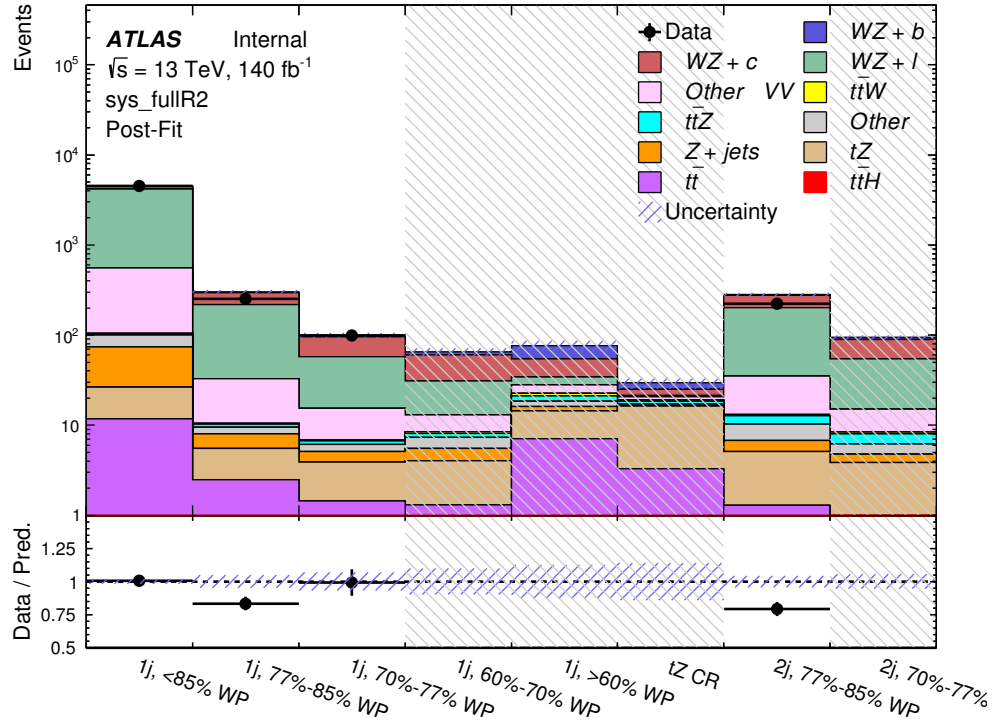


Figure 28: Post-fit summary of fit.

321 As described in section ??, there are 226 systematic uncertainties that are considered as NPs in
 322 the fit. These NPs are constrained by Gaussian or log-normal probability density functions. The
 323 latter are used for normalisation factors to ensure that they are always positive. The expected
 324 numbers of signal and background events are functions of the likelihood. The prior for each
 325 NP is added as a penalty term, decreasing the likelihood as it is shifted away from its nominal
 326 value.

327 The impact of each systematic uncertainty is calculated by performing the fit with the parameter
 328 of interest held fixed, varied from its fitted value by its uncertainty, and calculating $\delta\mu$ relative
 329 to the baseline fit. The impact of the most significant systematic uncertainties is summarized in
 330 table ??.

Uncertainty Source	$\Delta\mu$	
WZ + charm cross-section	-0.1966	0.2171
tZ cross-section	-0.1521	0.1518
WZ + light cross-section	0.1485	-0.1411
Other VV + b cross-section	-0.1115	0.1163
Flavor Tagging	0.0955	0.0957
Jet Energy Scale	0.0613	0.081
t <bar>t</bar>	-0.0662	0.0654
Luminosity	-0.0609	0.0655
Z + jets cross-section	-0.0284	0.0284
Other VV + charm cross-section	0.0207	-0.0202
Muon Trigger Scale Factor	0.019	0.0209
Total Systematic Uncertainty	0.3511	0.3679

Table 14: Summary of the most significant sources of systematic uncertainty.

³³¹ The ranking and impact of those nuisance parameters with the largest contribution to the overall
³³² uncertainty is shown in figure ??.

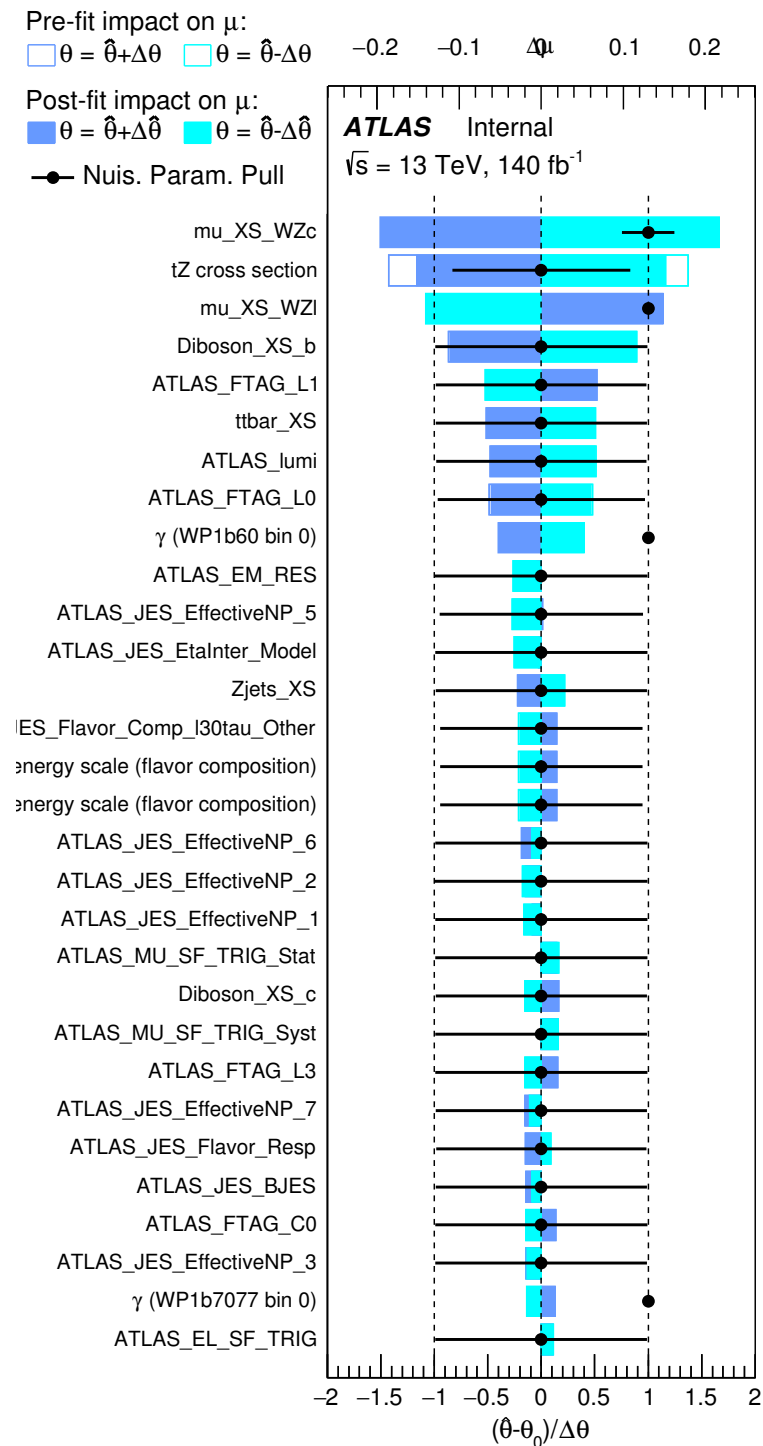


Figure 29: Impact of systematic uncertainties on the signal-strength of $WZ + b$

333 The large impact of the Jet Energy Scale and Jet Flavor Tagging is unsurprising, as the shape
 334 of the fit regions depends heavily on the modeling of the jets. The other major sources of
 335 uncertainty come from background modelling and cross-section uncertainty. The pie charts in
 336 figure ?? show that for the modelling uncertainties that contribute most correspond to the most
 337 significant backgrounds.

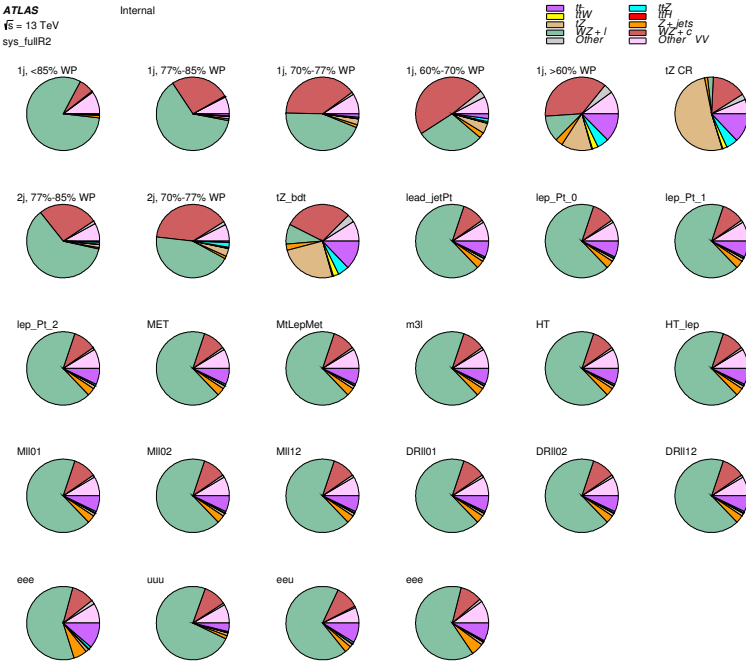


Figure 30: Background composition of the fit regions.

338 The correlations between these nuisance parameters are summarized in figure ??.

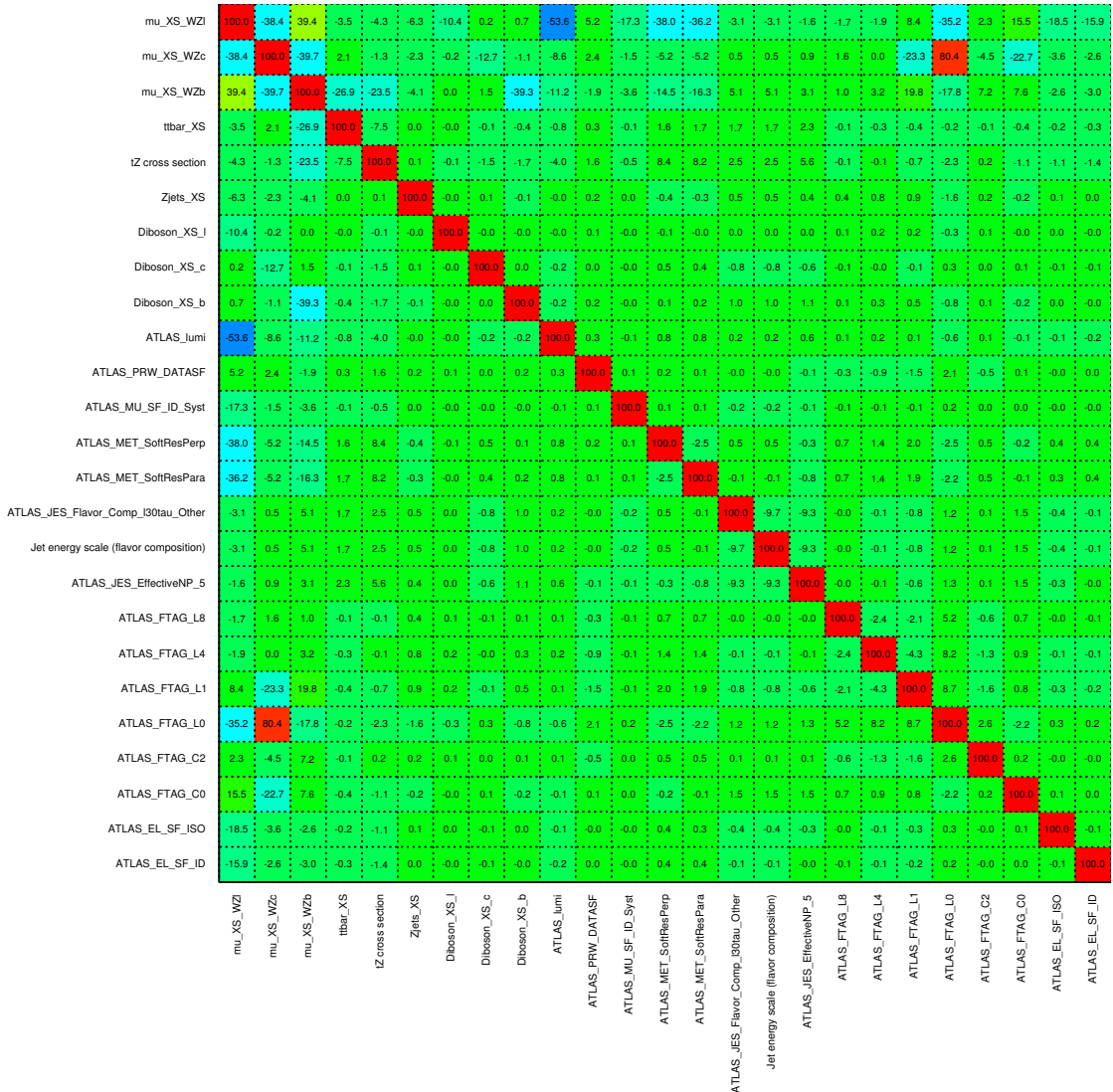


Figure 31: Correlations between nuisance parameters

339 The negative correlations between $\mu_{WZ+\text{charm}}$ and μ_{WZ+b} and $\mu_{WZ+\text{light}}$ are expected: WZ +
340 charm is present in both the WZ + b and WZ + light enriched regions, therefore increasing the
341 fraction of charm requires increasing the fraction of WZ + b and WZ + light. This reasoning
342 also explains the positive correlation between μ_{WZ+b} and $\mu_{WZ+\text{light}}$.

343 Two of the major backgrounds in the region with the highest purity of WZ + b are tZ and Other
344 VV + b, explaining the negative correlations between μ_{WZ+b} and the tZ cross section, and the
345 VV + b cross section.

346 The high correlation between the luminosity and $\mu_{WZ+light}$ arises from the fact that the uncer-
 347 tainty on $\mu_{WZ+light}$ is very low (around 4%). Small changes in luminosity cause a change in
 348 the yield of $WZ + light$ that is large compared to its uncertainty, producing a large correlation
 349 between these two parameters.

350 10 Conclusion

351 A measurement of $WZ +$ heavy flavor is performed using 140 fb^{-1} of $\sqrt{s} = 13 \text{ TeV}$ proton-
 352 proton collision data collected by the ATLAS detector at the LHC. **This section will be include**
 353 **final results once unblinded.**

354 References

- 355 [1] M. Aaboud et al. ‘Observation of electroweak $W^\pm Z$ boson pair production in association
 356 with two jets in pp collisions at $\sqrt{s} = 13 \text{ TeV}$ with the ATLAS detector’. In: *Phys.*
 357 *Lett.* B793 (2019), pp. 469–492. doi: [10.1016/j.physletb.2019.05.012](https://doi.org/10.1016/j.physletb.2019.05.012). arXiv:
 358 [1812.09740 \[hep-ex\]](https://arxiv.org/abs/1812.09740).
- 359 [2] T. Gleisberg et al. ‘Event generation with SHERPA 1.1’. In: *JHEP* 02 (2009), p. 007. doi:
 360 [10.1088/1126-6708/2009/02/007](https://doi.org/10.1088/1126-6708/2009/02/007). arXiv: [0811.4622 \[hep-ph\]](https://arxiv.org/abs/0811.4622).
- 361 [3] ATLAS Collaboration. *Electron efficiency measurements with the ATLAS detector using*
 362 *the 2015 LHC proton–proton collision data*. ATLAS-CONF-2016-024. 2016. URL: <https://cds.cern.ch/record/2157687>.
- 364 [4] ATLAS Collaboration. ‘Measurement of the muon reconstruction performance of the
 365 ATLAS detector using 2011 and 2012 LHC proton–proton collision data’. In: *Eur. Phys.*
 366 *J. C* 74 (2014), p. 3130. doi: [10.1140/epjc/s10052-014-3130-x](https://doi.org/10.1140/epjc/s10052-014-3130-x). arXiv: [1407.3935 \[hep-ex\]](https://arxiv.org/abs/1407.3935).
- 368 [5] *Evidence for the associated production of the Higgs boson and a top quark pair with the*
 369 *ATLAS detector*. Tech. rep. ATLAS-CONF-2017-077. Geneva: CERN, Nov. 2017. URL:
 370 <https://cds.cern.ch/record/2291405>.
- 371 [6] ATLAS Collaboration. *Jet Calibration and Systematic Uncertainties for Jets Reconstructed in the ATLAS Detector at $\sqrt{s} = 13 \text{ TeV}$* . ATL-PHYS-PUB-2015-015. 2015. URL:
 372 <https://cds.cern.ch/record/2037613>.
- 374 [7] ATLAS Collaboration. *Selection of jets produced in 13 TeV proton–proton collisions with*
 375 *the ATLAS detector*. ATLAS-CONF-2015-029. 2015. URL: <https://cds.cern.ch/record/2037702>.
- 377 [8] ATLAS Collaboration. ‘Performance of pile-up mitigation techniques for jets in pp col-
 378 lisions at $\sqrt{s} = 8 \text{ TeV}$ using the ATLAS detector’. In: *Eur. Phys. J. C* 76 (2016), p. 581.
 379 doi: [10.1140/epjc/s10052-016-4395-z](https://doi.org/10.1140/epjc/s10052-016-4395-z). arXiv: [1510.03823 \[hep-ex\]](https://arxiv.org/abs/1510.03823).

- 380 [9] ATLAS Collaboration. *Performance of missing transverse momentum reconstruction with*
381 *the ATLAS detector in the first proton–proton collisions at $\sqrt{s} = 13$ TeV*. ATL-PHYS-
382 PUB-2015-027. 2015. URL: <https://cds.cern.ch/record/2037904>.
- 383 [10] P. S. A. Hoecker. ‘TMVA 4 Toolkit for Multivariate Data Analysis with ROOT’. In: *arXiv:physics/0703039* (2013).
- 385 [11] F. Cardillo et al. ‘Measurement of the fiducial and differential cross-section of a top quark
386 pair in association with a Z boson at 13 TeV with the ATLAS detector’. In: ATL-COM-
387 PHYS-2019-334 (Apr. 2019). URL: <https://cds.cern.ch/record/2672207>.
- 388 [12] ATLAS Collaboration. ‘Luminosity determination in pp collisions at $\sqrt{s} = 7$ TeV using
389 the ATLAS detector at the LHC’. In: *Eur. Phys. J. C* 71 (2011), p. 1630. doi: [10.1140/epjc/s10052-011-1630-5](https://doi.org/10.1140/epjc/s10052-011-1630-5). arXiv: [1101.2185 \[hep-ex\]](https://arxiv.org/abs/1101.2185).
- 391 [13] G. Aad et al. ‘Jet energy resolution in proton-proton collisions at $\sqrt{s} = 7$ TeV recorded
392 in 2010 with the ATLAS detector’. In: *The European Physical Journal C* 73.3 (Mar.
393 2013), p. 2306. issn: 1434-6052. doi: [10.1140/epjc/s10052-013-2306-0](https://doi.org/10.1140/epjc/s10052-013-2306-0). URL:
394 <https://doi.org/10.1140/epjc/s10052-013-2306-0>.
- 395 [14] A. Collaboration. ‘Performance of b -jet identification in the ATLAS experiment’. In: *Journal of Instrumentation* 11.04 (2016), P04008. URL: <http://stacks.iop.org/1748-0221/11/i=04/a=P04008>.